

Plasma phenomena in nanostructures and neutron stars

Scientific session of the Physical Sciences Division of the Russian Academy of Sciences (26 March 2008)

V V Klimov; Ya N Istomin; Yu A Kosevich

DOI: 10.1070/PU2008v051n08ABEH006794

A scientific session of the Physical Sciences Division of the Russian Academy of Sciences (RAS) was held on 26 March 2008 at the conference hall of the P N Lebedev Physical Institute, RAS. The following reports were presented at the session:

(1) **Klimov V V** (P N Lebedev Physical Institute, RAS, Moscow) “Nanoplasmonics”;

(2) **Istomin Ya N** (P N Lebedev Physical Institute, RAS, Moscow) “Electron–positron plasma generation in the magnetospheres of neutron stars”;

(3) **Kosevich Yu A** (N N Semenov Institute of Chemical Physics, RAS, Moscow) “Multichannel propagation and scattering of phonons and photons in low-dimension nanostructures”.

An abridged version of these reports is given below.

PACS numbers: 61.46.Bc, 71.45.Gm, **81.07. – b**
DOI: 10.1070/PU2008v051n08ABEH006595

Nanoplasmonics

V V Klimov

Advances in the production and visualization of nano-sized clusters and other metal nanoparticles (Fig. 1) have given rise to nanoplasmonics, an important and fast-developing area of nanotechnology and nanooptics. Aimed at designing complex optical nanodevices, nanoplasmonics studies phenomena related to oscillations of conduction electrons in metal nanostructures and nanoparticles and how these oscillations interact with light, atoms, and molecules. Plasmon oscillations in nanoparticles differ considerably from surface plasmons [1] and are therefore called localized plasmons.

What is most special about nanoplasmonic phenomena is that the strong spatial localization of the electronic oscillations is combined with their high frequencies varying from UV to IR ranges. The strong localization, in turn, leads to a huge strengthening of local optical and electric fields. Finally, the properties of localized plasmons are critically dependent on the nanoparticle shape, enabling their resonance systems

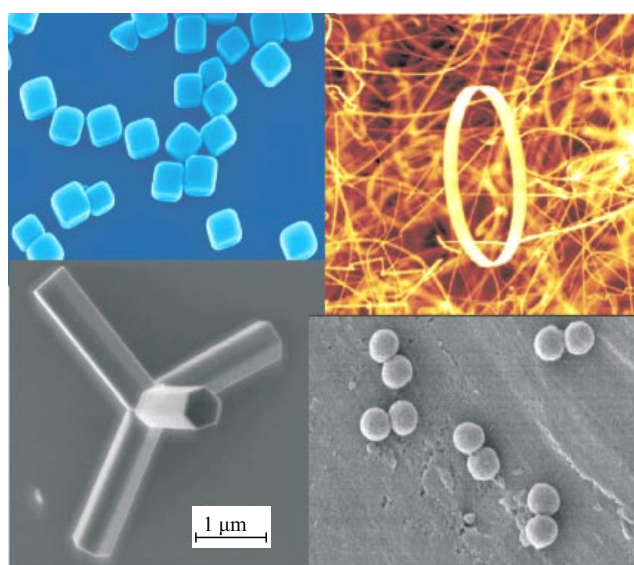


Figure 1. Examples of nanoparticles amenable to efficient synthesis techniques.

to be tuned so as to effectively interact with light or with elementary quantum systems like molecules and quantum dots.

These most important properties of plasmon nanoparticles have already allowed a range of new effects to be detected. First and foremost, the huge local fields that arise near nanoparticles lead to an increase of 10–14 orders of magnitude in the Raman scattering cross section, conceivably making individual molecule detection possible [2, 3]. The presence of local fields can be exploited to design marker-free techniques for determining the structure of DNA [4]. Using the complex spectral structure of plasmon nanoparticles, it proves possible to simultaneously enhance their light absorption and light emission properties, giving rise to high-performance fluorophores and nano-sized light sources [5]. Also, there are suggestions to use plasmon nanoparticles in the SPASER (Surface Plasmon Amplification by Stimulated Emission of Radiation) context [6]. Other than the above novel applications — ones that rely on plasmon nanoparticle physics — achievements in the field of nanoplasmonics can be used to improve the performance-to-cost ratio of, for example, solar batteries and LEDs. Furthermore, the small size of metal nanostructures combined with optically fast

processes occurring in them gives nanoplasmonics good promise for developing a new component base for computers and data processing devices [7].

Exactly how a localized plasmon should be defined is as yet an unsettled question, but a widely held view is that this is simply a resonance peak in the nanoparticle's light-scattering or light-absorption cross sections. This is often misleading though, because far from all localized plasmons can be readily detected or described as such ('dark' plasmons with zero dipole polarizability being an example). In our view, the term 'a localized plasmon' should be applied to the solutions of the problem covering free quasistatic oscillations in nanoparticles (the term 'free' meaning the absence of exciting fields), which reduces to the following Laplace equation boundary value problem:

$$\Delta\varphi_n^{\text{in}} = 0, \quad \Delta\varphi_n^{\text{out}} = 0, \quad \varepsilon_n \frac{\partial\varphi_n^{\text{in}}}{\partial\mathbf{n}} \Big|_S = \frac{\partial\varphi_n^{\text{out}}}{\partial\mathbf{n}} \Big|_S, \quad (1)$$

where φ_n^{in} and φ_n^{out} are the electric potentials of the plasmon eigenfunctions inside and outside of the particle, respectively, and $\partial\varphi_n/\partial\mathbf{n}|_S$ denotes the normal derivative at the boundary of the particle. The last of equations (1) ensures the fulfilment of a continuity condition of normal induction components. The mathematical complexity of the seemingly simple system (1) is enormous, as is the range of physical problems it encompasses.

It is the eigenfunctions $\mathbf{e}_n = -\nabla\varphi_n$ and eigenvalues ε_n of the permittivity that determine a localized plasmon oscillation. For finite-sized nanoparticles, the eigenvalues ε_n assume only negative (with zero imaginary part) discrete values, making localized plasmons very similar in this respect to ordinary atoms and molecules. What is extremely important here is that *the eigenvalues ε_n are of no relevance to the permittivity of the real material the nanoparticles are made of.*

Numerical studies of localized plasmons are conveniently carried out by using Eqn (1) in its integral form:

$$\sigma(\mathbf{r}) = \frac{1}{2\pi} \frac{\varepsilon - 1}{\varepsilon + 1} \int_S d^2\mathbf{r}' \sigma(\mathbf{r}') \frac{\mathbf{n}(\mathbf{r})(\mathbf{r} - \mathbf{r}')}{|\mathbf{r} - \mathbf{r}'|^3}, \quad \mathbf{r}, \mathbf{r}' \in S, \quad (2)$$

where $\sigma(\mathbf{r})$ is the surface charge, $\mathbf{n}(\mathbf{r})$ is the outer normal to the particle's surface, and the integration is taken over the surface of the particle.

Once the solution of quasistatic problem (1) or (2) has been found, the solution of the actual problem with given exciting fields $\mathbf{E}^0(\mathbf{r})$ can be expressed in terms of the eigenfunctions and eigenvalues of the permittivity of localized plasmons as follows:

$$\mathbf{E}(\mathbf{r}, \omega) = \mathbf{E}^0(\mathbf{r}, \omega) + \sum_n \mathbf{e}_n(\mathbf{r}) \frac{[\varepsilon(\omega) - 1]}{[\varepsilon_n - \varepsilon(\omega)]} \frac{\int_V \mathbf{e}_n \mathbf{E}^0 dV}{\int_V \mathbf{e}_n^2 dV}, \quad (3)$$

where the integration is taken over the volume V of the particle, and $\varepsilon(\omega)$ is the frequency-dependent permittivity of the actual material of the nanoparticle. At those frequencies ω_n for which some of the denominators is close to zero, $\varepsilon_n \approx \varepsilon(\omega_n)$, a plasmon resonance occurs, which can, in principle, be observed. In the case of the Drude dispersion, the resonance plasmon frequencies can be found from the relationship

$$\omega_n = \frac{\omega_p}{\sqrt{1 - \varepsilon_n}}, \quad (4)$$

where ω_p is the plasmon frequency of the metal. From Eqn (3), in turn, the polarizabilities, scattering and absorption cross sections, spontaneous emission rates of the atoms, etc. can be found.

The most important feature of quasistatic description (1) is that it narrows the problem to plasmon oscillations alone. Other particle's modes (whispering gallery modes) do not arise in this picture and so do not hamper obtaining and interpreting the results.

In fact, the above theory applies only to nanoparticles, i.e., when retardation effects are negligible. If the nanoparticles are considered to be finite in comparison with the wavelength, the eigenvalues ε_n acquire negative imaginary parts which are related to the emission of the plasmons and are given by

$$\Delta\varepsilon_m = -ik^3 \frac{(\varepsilon_m - 1)^2}{6\pi} \frac{(\int_V \mathbf{e}_m dV)^2}{\int_V \mathbf{e}_m^2 dV}. \quad (5)$$

In the simplest case of spherical nanoparticles of radius R_0 , the problem for the eigenfunctions and eigenvalues of the permittivity has the solution

$$\varepsilon_n = -\frac{n+1}{n} - A_n(ka)^2 - 2i(ka)^3 \delta_{n1} + \dots, \quad n = 1, 2, 3, \dots, \quad (6)$$

$$A_1 = -\frac{12}{5}, \quad A_2 = -\frac{5}{14}, \quad A_3 = -\frac{56}{405}, \quad \dots, \quad \varphi_{\text{in}} = \left(\frac{r}{R_0}\right)^n Y_n^m(\theta, \varphi), \quad \varphi_{\text{out}} = \left(\frac{R_0}{r}\right)^{n+1} Y_n^m(\theta, \varphi), \quad (7)$$

where r is the radius, and Y denotes spherical harmonics. The most important electron oscillation mode is the dipole mode, with $n = 1$, and $\varepsilon_1 = -2$.

For more composite and less symmetric nanoparticles, the resonance plasmon frequencies and the potentials of plasmon atoms have a more intricate form. For example, in the case of a metal nanoparticle in the form of a three-axis ellipsoid with half-axes $a_1 > a_2 > a_3$, the plasmon frequencies will be given by [8]

$$\varepsilon_{nm}(a_1, a_2, a_3) = \frac{E_n^m(a_1) F_n^m(a_1)}{E_n^m(a_1) F_n^m(a_1)}, \quad n = 1, 2, 3, \dots, \quad m = 1, 2, \dots, 2n+1, \quad (8)$$

where E_n^m and F_n^m are the internal and external Lamé functions, and the prime denotes the derivative of a function with respect to its argument.

The nanoparticles of most practical importance are those having the shape of a cube—or rather being close to this shape, because the edges and tips of such nanoparticles are rounded off in the growth process [9] (see Fig. 1). Localized plasmons in this kind of nanoparticles are conveniently discussed by representing their surface parametrically in the form

$$x^n + y^n + z^n = a^n. \quad (9)$$

Here, $n = 2$ and $n = \infty$ correspond to a sphere and a cube, respectively.

The dependences of the resonance values of the permittivity on the parameter n are depicted in Fig. 2. It is seen how the permittivity eigenvalues split and gradually transform into

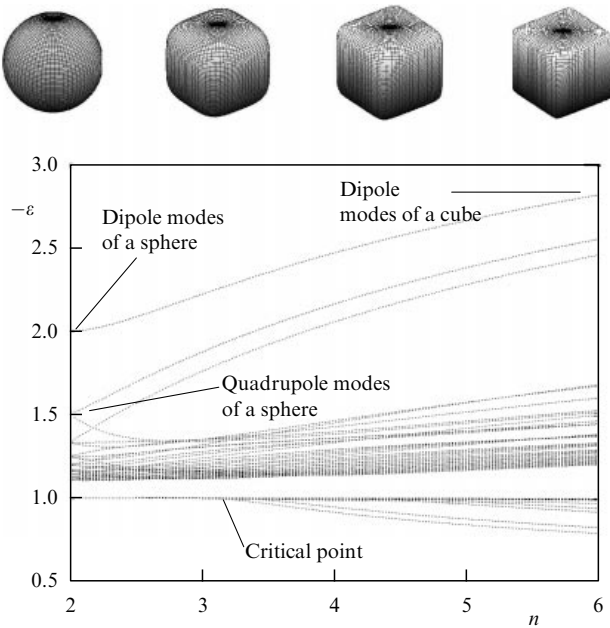


Figure 2. Spectrum of plasmon oscillations as a function of the shape of nanoparticles with cubic morphology.

those of a cube as the symmetry alters. Remarkably, at $n=2.5$ the plasmon spectrum branches with $\varepsilon > -1$ form, which are characteristic of a cube but not of a sphere. In fact, the plasmon spectra experience a phase transition at $n=2.5$. A similar transition often occurs in other complex-shaped nanoparticles, as well. The spectra obtained are very important in providing pure spectroscopic means with which the shape-changing processes of nanoparticle crystallization or melting can be controlled.

Plasmon oscillations in a cluster comprising two spherical nanoparticles provide another impressive example of localized plasmons [10–12].

The full spectrum of plasmon oscillations we obtained for this system is depicted in Fig. 3. The region $\omega < \omega_p/\sqrt{2}$ ($\varepsilon < -1$) exhibits only symmetric and antisymmetric hybrid states which exist for any interparticle distances and which in the limit of large distances between nanospheres change in a

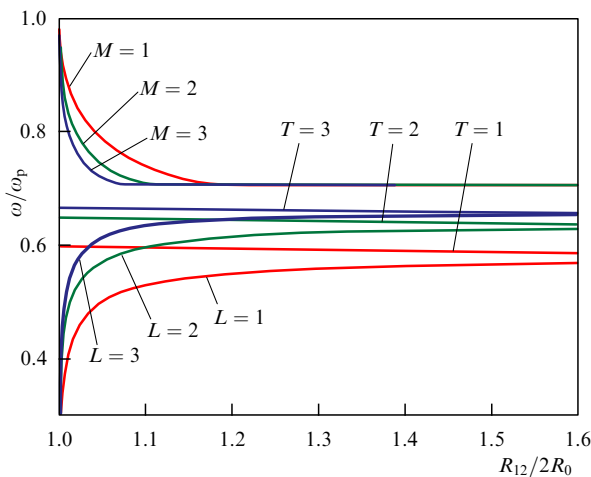


Figure 3. Plasmon oscillation spectrum for a two-nanosphere cluster versus the separation R_{12} ($m=1$) between the spheres.

continuous manner to the corresponding states of weakly interacting localized plasmons with characteristics described by formulas (6), (7). It is these hybrid states which were studied in Refs [13–15].

In the region of $\omega_p \geq \omega > \omega_p/\sqrt{2}$ ($0 > \varepsilon > -1$), however, plasmon oscillations are only possible for small [$R_{12}/(2R_0) < 1.2$] distances between the nanoparticles. At these distances, similar to nanoparticles of cubic morphology, the plasmon spectra of a two-nanoparticle cluster also show a phase transition.

In the region of small distances between nanospheres, the new branch of localized plasmon oscillations (M modes or plasmon molecules) has properties amenable to an analytical description [10–12]:

$$\varepsilon_m^M = -(M + m + \delta_m) \cosh \frac{R_{12}}{2R_0} + \dots, \quad (10)$$

$$M = 1, 2, 3, \dots, \quad m = 0, 1, 2, \dots,$$

where R_{12} is the center-to-center distance between the spheres, and

$$\delta_0 = \frac{1}{2}, \quad \delta_1 = -0.08578, \quad \delta_2 = -0.2639,$$

$$\delta_3 = -0.33, \dots, \quad \delta_\infty = -\frac{1}{2}, \quad (11)$$

$$\delta_m = -\frac{1}{2} - \frac{1}{2m} + \frac{1}{8m^3} - \frac{1}{16m^5} + \frac{5}{128m^7} - \dots \quad (m > 0).$$

Large azimuthal numbers, $m \gg 1$, also allow simple asymptotic expressions to be obtained for the plasmon oscillation spectra of a two-sphere cluster, and the eigenfunctions of localized plasmons can also be expressed analytically in the small separation limit [10–12].

Figure 4 plots the spatial distribution in the xz plane of the wave function (potential) of localized plasmons.

In the axisymmetric ($m=0$) case there is a qualitative correspondence between the spatial structure of the antisymmetric (L modes) and symmetric (T modes) plasmon oscillations and that of the wave functions of isolated spherical nanoparticles, namely, the positive charge resides on one hemisphere, whereas a negative charge of the same amount (note the sphere electroneutrality requirement) locates at the opposite part of the sphere. In this case, interactions between plasmon atoms simply boil down to a certain redistribution of charge over opposite hemispheres.

In the case of symmetric M modes appearing due to the phase transition, the situation is directly opposite and the charges concentrate in a small region close to the gap between the nanospheres. At those points on the spheres that are distant from the gap, the wave functions of plasmon molecules (M modes) become essentially zero.

As the distance between the nanospheres increases, the symmetric M modes become less localized—to eventually disappear at a critical distance, whereas the antisymmetric (L) and symmetric (T) modes remain unchanged as far as their localization is concerned.

The difference in localization between symmetric M modes, on the one hand, and the antisymmetric L modes and symmetric T modes, on the other, results in the former and the latter responding fundamentally differently to exciting fields. The L and T modes have a polarizability of the order of the nanosphere volume, $\alpha \sim R_0^3$, and interact effectively with uniform external fields of proper orientation

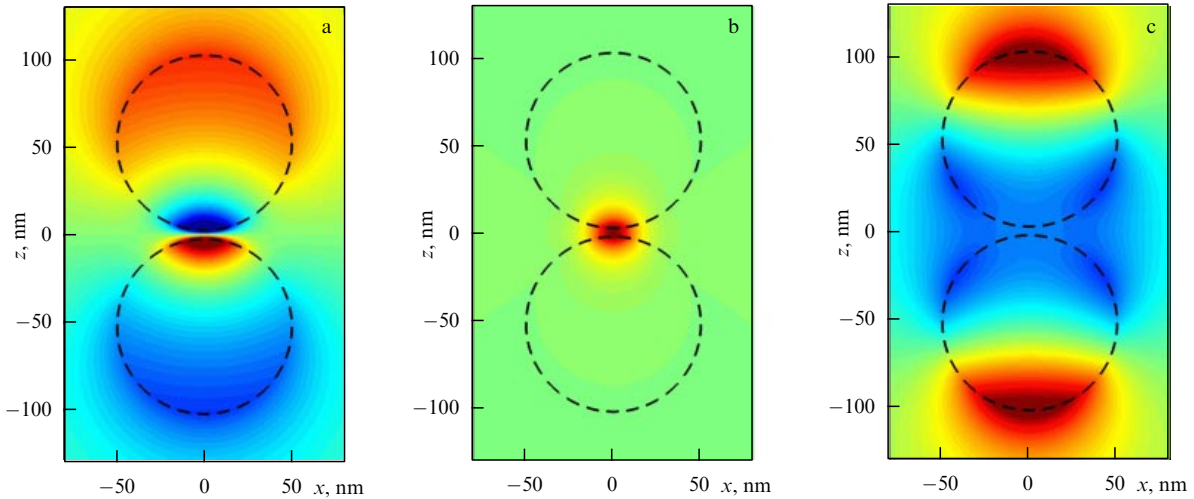


Figure 4. Spatial distribution of electric potential for (a) L modes, (b) M modes, and (c) T modes ($L, M, T = 1$) in the xz plane [$m = 0, R_{12}/(2R_0) = 1.05$].

and symmetry. M modes (plasmon molecules), in contrast, possess relatively low polarizability $\alpha \sim \Delta^3$, where Δ is the gap between the spheres, so their excitation by uniform optical fields is weak compared to the L and T modes. On the other hand, M modes interact effectively with strongly nonuniform fields that are localized near the sphere–sphere gap and arise due to the emission of atoms and molecules resided near the gap.

The discussion above was concerned with localized plasmons in a cluster comprising two identical nanospheres. The same localized plasmons also exist in clusters of two different nanospheres or two different bubbles in metal. For example, the spectrum of plasmon oscillations for two different spheres a small distance apart can be described by the expression

$$\frac{\varepsilon_1(\omega) - \varepsilon_3}{\varepsilon_1(\omega) + \varepsilon_3} \frac{\varepsilon_2(\omega) - \varepsilon_3}{\varepsilon_2(\omega) + \varepsilon_3} \approx \exp[(2N + 2m - 1)(\eta_2 - \eta_1)], \quad (12)$$

$$N = 1, 2, 3, \dots, \quad m = 0, 1, 2, \dots,$$

where the parameter $\eta_2 - \eta_1$ can be found from the relationship

$$\cosh(\eta_2 - \eta_1) = \frac{R_{12}^2 - R_1^2 - R_2^2}{2R_1 R_2}, \quad (13)$$

and $\varepsilon_1, \varepsilon_2, \varepsilon_3$ are the permittivities of the first sphere, the second sphere, and the region in-between, respectively.

The strong localization of M modes suggests that what mainly determines their properties is the radii of curvature of the two almost touching surfaces and the distance between their centers. Therefore, for any smooth nonspherical particles the properties of M modes that form in the gap between them can be estimated by considering M modes in two spheres approximating the nonspherical particles at their point of contact.

Two closely spaced semi-infinite bodies give rise to a more complex situation because in this case some of the charges can move arbitrarily far from the region of contact and the spectrum becomes continuous—with the result that localized plasmons do not, strictly speaking, exist in such systems. However, stable plasmon oscillations similar to antisym-

metric L modes and symmetric M modes exist in this case, as well [12].

As already noted, the unique properties of localized plasmons—nanolocalization, optical frequencies, shape-tuned resonances—are of interest for many applications.

Also, the strong localization of M modes appears to show promise for a range of applications, especially those relying on the effective interaction of nanolocalized light sources (molecules and nanocrystalline quantum dots) with nanoparticles and nanostructures, and for nanoelectromechanical devices [16] where van der Waals forces are of importance.

As is known, van der Waals forces relate to the spatial dependence of vacuum-fluctuation energy density. In the case of closely spaced plasmon nanoparticles, the van der Waals energy is dominated by contributions from the zero-point oscillations of localized plasmons.

For two identical plasmon nanospheres, the van der Waals energy consists of contributions from the zero-point oscillations of antisymmetric L modes and symmetric T and M modes:

$$U_{\text{vdW}} = \frac{\hbar}{2} \left(\sum_{M=1}^{\infty} \omega_{M0} + \sum_{L=1}^{\infty} \omega_{L0} + \sum_{T=1}^{\infty} \omega_{T0} \right) + \hbar \left(\sum_{M,m=1}^{\infty} \omega_{Mm} + \sum_{L,m=1}^{\infty} \omega_{Lm} + \sum_{T,m=1}^{\infty} \omega_{Tm} \right). \quad (14)$$

Although the contributions from different modes are given by formally identical expressions, the physical consequences they produce are totally different. It is seen from Fig. 3 that the energies (frequencies) of antisymmetric states (L modes) increase with intersphere distance, leading to attraction between the particles. In contrast, the energy of M modes decreases with distance, making the nanospheres repel. Symmetric T modes also give rise to a very weak repulsion.

The plot in Fig. 5, obtained in Ref. [17] by directly summing all the modes in Eqn (14), shows the way in which contributions from various plasmonic states to the van der Waals energy vary with the separation between the spheres. As expected, the symmetric and longitudinal antisymmetric modes lead, respectively, to the repulsion and attraction of nanoparticles. It turned out unexpected that

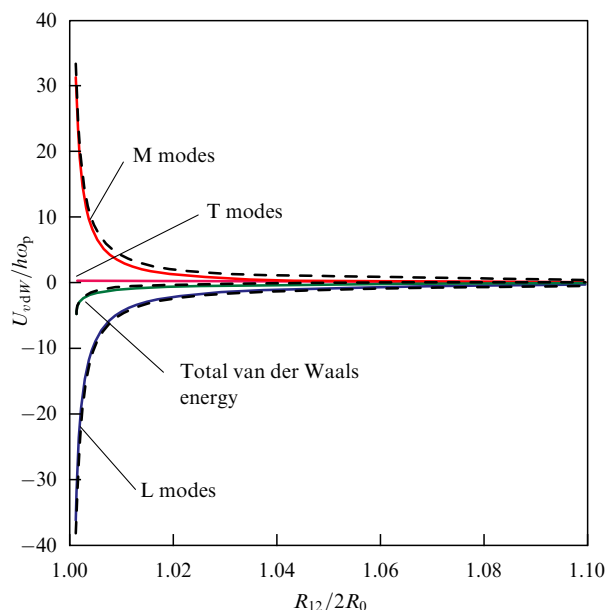


Figure 5. Van der Waals energy due to various plasmonic states as a function of separation between the spheres.

the repulsive contribution due to M modes is nearly equal to the attractive contribution caused by L modes. As a result, the total van der Waals energy increases with separation between the spheres—which reveals its attractive nature—but is an order of magnitude smaller than would be obtained by ignoring the M modes we discovered.

The direct measurement of van der Waals forces between plasmon nanoparticles provides a basis for experimentally verifying the existence of plasmon molecules (M modes).

The fact that M modes very effectively interact with strongly nonuniform fields suggests that optical interaction between molecules and M modes can be used in developing various single-molecule detectors or quantum dots. Figure 6 depicts the emission wavelength dependence of the radiative spontaneous decay rate of various kinds of molecules residing in the gap between two nanoparticles. The nanoparticles are taken to be made either of Na atoms with plasmon resonances in the optical region (Fig. 6a) or of SiC with phonon–polariton resonances in the infrared region (Fig. 6b). The peaks on the right-hand side of Fig. 6 correspond to the interaction of an ordinary molecule with T modes, whereas those on the left correspond to the interaction of localized plasmons with M modes.

Inspection of Fig. 6 shows that, similarly to the case of the van der Waals energy, the interaction with M modes is of more significance than that with symmetric T modes. It is also of extreme importance that a uniform external field is inefficient for exciting M modes (plasmon molecules), meaning that efficient single-molecule nanodetectors can be developed by using two-, or more, nanosphere clusters with geometry allowing excitation of plasmon molecules with a fixed frequency. These nanodetectors cannot practically be excited by external fields having the oscillation frequency of the M modes and will therefore have a high signal-to-noise ratio.

On the other hand, the effective interaction of plasmon molecules with ordinary atoms and molecules can be employed to develop SPASER and nanolaser type devices for operating singly or in a lattice.

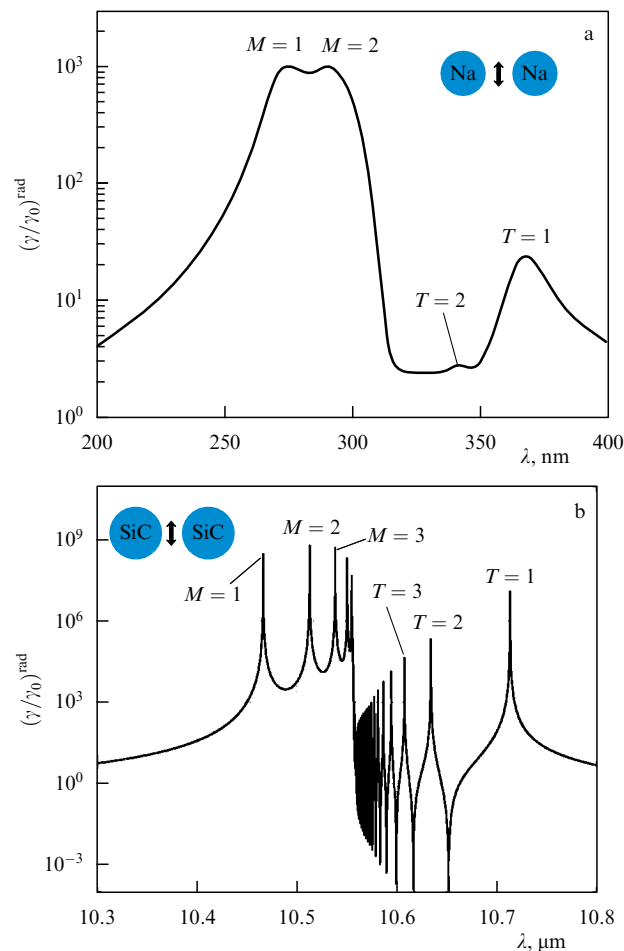


Figure 6. Relative radiative spontaneous decay rate of a molecule residing in the gap between two nanospheres as a function of the molecule's emission wavelength for (a) an Na nanosphere [18], and (b) an SiC nanosphere [19]. In either case, $R_{12}/(2R_0) = 1.5$. The dipole moment of the atom is directed as shown by the arrow.

To summarize, this report presents the general theory and the results of investigation of plasmon oscillations in separate nanoparticles and nanoparticle clusters. It was demonstrated that changing the shape of nanoparticles causes radical changes—specifically, plasmon phase transitions—in the spectra of localized plasmons. It was shown that the localized plasmons discussed in this report are an important concept for describing nanoelectromechanical systems and single-molecule nanodetectors, as well as for spectroscopically monitoring the shape of nanoparticles in the process of their synthesis.

Whereas this report was concerned with localized plasmons in nanoparticles of ordinary materials with $\varepsilon < 0$, much recent attention has been focused on metamaterials with both permittivity and permeability being negative [20]. Localized plasmons in nanoparticles produced from such materials have important differences from those discussed here [21] and can therefore naturally be called metaplasmons.

Acknowledgments. The author gratefully acknowledges the financial support provided by the Russian Foundation for Basic Research (grants Nos 05-02-19647, 07-02-01328) and the RAS Presidium.

References

1. Raether H *Surface Plasmons on Smooth and Rough Surfaces and on Gratings* (Berlin: Springer-Verlag, 1988)
2. Moskovits M et al., in *Optical Properties of Nanostructured Random Media* (Topics in Applied Physics, Vol. 82, Ed. V M ShalaeV) (Berlin: Springer-Verlag, 2002) p. 215
3. Wang Z et al. *Proc. Natl. Acad. Sci. USA* **100** 8638 (2003)
4. Lakowicz J R et al. *J. Phys. D: Appl. Phys.* **36** R240 (2003)
5. Guzatov D V, Klimov V V *Chem. Phys. Lett.* **412** 341 (2005)
6. Bergman D J, Stockman M I *Phys. Rev. Lett.* **90** 027402 (2003)
7. Zia R et al. *Mater. Today* **9** (7–8) 20 (2006)
8. Klimov V V, Guzatov D V “*Opticheskie svoistva trekhosnogo nanoellipsoida i ikh vliyanie na izluchenie atomov i molekul*” (“Plasmon oscillations in ellipsoidal nanoparticles: beyond dipole approximation”) (in preparation)
9. Sun Y, Xia Y *Science* **298** 2176 (2002)
10. Klimov V V, Guzatov D V *Phys. Rev. B* **75** 024303 (2007)
11. Klimov V V, Guzatov D V *Kvantovaya Elektron.* **37** 209 (2007) [*Quantum Electron.* **37** 209 (2007)]
12. Klimov V V, Guzatov D V *Appl. Phys. A* **89** 305 (2007)
13. Claro F *Phys. Rev. B* **25** 7875 (1982)
14. Ruppin R *Phys. Rev. B* **26** 3440 (1982)
15. Nordlander P et al. *Nano Lett.* **4** 899 (2004)
16. Ekinci K L, Roukes M L *Rev. Sci. Instrum.* **76** 061101 (2005)
17. Klimov V V, Lambrecht A, arXiv:0712.4067
18. Palik E D (Ed.) *Handbook of Optical Constants of Solids* (Orlando: Academic Press, 1985)
19. Engelbrecht F, Helbig R *Phys. Rev. B* **48** 15698 (1993)
20. Soukoulis C M, Linden S, Wegener M *Science* **315** 47 (2007)
21. Klimov V V *Opt. Commun.* **211** 183 (2002)

PACS numbers: 52.27.Ep, 97.10.Ld, 97.60.Jd
DOI: 10.1070/PU2008v051n08ABEH006596

Electron – positron plasma generation in the magnetospheres of neutron stars

Ya N Istomin

1. Introduction

In this report we discuss the processes of the generation of relativistic electron – positron plasma in magnetospheres of rotating magnetized neutron stars. Both not very strong magnetic fields, $B \simeq 10^{12}$ G, typical for radio pulsars, and superstrong magnetic fields, $B \simeq 10^{14} - 10^{15}$ G, typical for so-called magnetars, are considered. It is shown that superstrong magnetic fields do not suppress particle production. Intervals of neutron star parameters, first of all rotation periods and magnetic field strengths, allowing effective plasma generation have been found.

Neutron stars are the smallest observed stars in the Galaxy. Their radius R is around 10 km (for comparison, the solar radius amounts to 7×10^5 km). So, the ratio of the radius of a neutron star to that of ordinary stars is about 10^{-5} . However, with such a small radius, neutron stars have a mass M on the order of the solar one M_\odot , with the average magnitude being $1.4M_\odot$. The mean density of the neutron star matter is $\bar{\rho} = 3M/4\pi R^3 = 7 \times 10^{14}$ g cm $^{-3}$, which exceeds the standard nuclear density $\rho_0 = 2.8 \times 10^{14}$ g cm $^{-3}$ by several times ($\bar{\rho} \simeq 2.5\rho_0$). Therefore, a neutron star can be considered as a huge atomic nucleus with a radius of about 10 km. The matter density at the center of the star can exceed the nuclear one by 10–20 times. At such densities in the neutron star center, pion, hyperon, and kaon condensations

are made possible. The possibility of the appearance of quarks, mostly strange, is also discussed. Such stars are termed strange stars.

The body of a neutron star consists of outer and inner crusts, where the neutronization of matter occurs, and of outer and inner cores. The number of protons and electrons in the inner crust and outer core is much smaller than the number of neutrons, the ratio being of the order of several percent. Neutrons and protons probably form superfluid and superconducting pairs, so that neutron star matter possesses superfluid and superconductive properties. It should also be noted that the gravitational energy of a neutron star amounts to a substantial fraction of its rest energy: $E_g = GM^2/R \simeq 5 \times 10^{53}$ erg = $0.2Mc^2$, where G is the Newtonian constant of gravitation.

The existence of neutron stars was predicted by Baade and Zwicky [1] in 1934, two years after the discovery of neutrons. Despite their small size, neutron stars are among the most active stars, radiating energy in the entire electromagnetic spectral range from radio waves to ultra-high energy photons beyond 1 TeV.

Neutron stars were discovered in 1967 by Bell and Hewish [2] as sources of periodic radio emission — radio pulsars. In 1974, Hewish was awarded the Nobel Prize in Physics for his decisive role in the discovery of pulsars.

Presently, more than 1500 radio pulsars are known. Their pulse-repetition intervals, i.e., the periodicity of recurring radio pulses, are very stable and span the range from 1.5 ms to 8.5 s. The high stability and small intervals can only be explained by the rotation of a small body with radius $R < 5 \times 10^7$ cm. Only neutron stars have such small radii. A constant increase in the pulse-repetition intervals P of radio pulsars with time is also observed, $dP/dt \simeq 10^{-15}$ s s $^{-1}$, implying a loss in the rotational energy of a neutron star. The measured energy loss $dE/dt = (2\pi)^2 IP^{-3} dP/dt$ for the standard moment of inertia $I = 10^{45}$ g cm 2 of a neutron star is on the order of $dE/dt \simeq 4 \times 10^{31}$ erg s $^{-1}$. However, rapidly rotating neutron stars actually lose much higher energy. For example, the Crab Nebula pulsar emits 10^{38} erg s $^{-1}$, which is by many orders higher than the solar luminosity. The energy emitted in the radio frequency band amounts to only a tiny fraction, $10^{-5} - 10^{-6}$, of the total energy losses. The most powerful radio pulsars also radiate in other spectral ranges, including the optical, X-ray, and gamma-ray ranges. The emission power increases with frequency, but nevertheless remains much smaller than the total energy losses. The question arises as to what is mainly emitted by a rotating neutron star?

In addition to being radio pulsars, neutron stars are also the sources of

(a) powerful X-ray emission, both periodic (X-ray pulsars) and irregular. These are neutron stars in close binary stellar systems in which the star-companion provides the neutron star with matter accreting onto it. The energy liberated during accretion amounts to $\simeq 0.2$ of the rest energy of the infalling flux of matter;

(b) gamma- and X-ray bursts. These are anomalous X-ray pulsars (AXPs) and soft gamma repeaters (SGRs). Both these groups are combined into one class of the so-called magnetars. They comprise neutron stars with ultrahigh surface magnetic fields of $10^{14} - 10^{15}$ G;

(c) steady X-ray emission from central compact objects (CCOs) in supernova remnants. These are neutron stars formed during the core collapse of pre-supernova stars;

(d) very faint optical emission. These are nearest radio-quiet isolated neutron stars;

(e) sporadic radio bursts from rotating radio transients (RRATs). These are neutron stars which are not steady working radio pulsars;

(f) unusual gamma- and X-ray emission from sources like Geminga (Gemini gamma-ray source).

The study of neutron stars solves and provides the possibility to solve a number of fundamental physical problems. These include first of all the analysis of the equation of state of superdense matter with $\rho > \rho_0$. The equation of state (up to now, more than ten different equations of state have been proposed theoretically) determines the form of the dependence $M(R)$ of the mass M of a neutron star on its radius R . Masses of neutron stars are measured with a good accuracy in binary systems, their radii being inferred from intensity measurements of the emission from the neutron star surface. Up to the present, however, the accuracy of measurements of radii and masses of neutron stars has been insufficient for the unique determination of the equation of state of the superdense matter.

The superfluidity of neutron matter can be examined by measuring interruptions in the rotation period of a radio pulsar during neutron star rotation braking (glitch). In some cases, the interruption dynamics is explained well by the unpinning of a superfluid vortex from the stellar core. The evolution of the magnetic field 'frozen' in the star allows conclusions about the superconductivity in the neutron star core.

In strong magnetic fields B pertinent to neutron stars, $B > 10^{12}$ G, the structure of matter is unusual. In such fields, the cyclotron radius of atomic electrons is smaller than the Bohr radius, and the atoms are strongly compressed in the direction perpendicular to the magnetic field and take the form of a needle. The properties of matter formed by such atoms can be judged from the interaction of the neutron star surface, where the matter density reaches 10^5 g cm $^{-3}$, with its magnetosphere.

Very importantly, observations of neutron stars as radio pulsars allow the checking of General Relativity through measurements of post-Newtonian corrections to the dynamics of motion of two neutron stars in a close binary system. For example, a measured decrease in the orbital period of the pulsar PSR B 1913+16 amounted to $dP_{\text{orb}}/dt = -2.4086 \times 10^{-12}$ s s $^{-1}$, which corresponds to a decrease in the binding energy of the stars due to their emission of gravitational waves. In 1993, R A Hulse and J H Taylor, Jr. were awarded the Nobel Prize in Physics for the discovery of a new type of pulsar, a discovery that has opened up new possibilities for the study of gravitation. The timing, i.e., the precise measurement of the time of arrival of individual pulses, is now so accurate that several of the most stable radio pulsars can be used to construct a frequency standard more stable than current atomic clocks. Measurements of the retardation of a radio signal at different frequencies and its polarization are used to determine the parameters of interstellar medium: the electron number density, the magnetic field strength, and inhomogeneities. By this is meant that it is also possible to probe the nearby environments of radio pulsars. The timing of radio pulsars allows studies of the cosmic background of gravitational waves.

Finally, observations of active neutron stars enable us to investigate electrodynamic processes in superstrong magnetic

fields $B > 10^{12}$ G typical for neutron stars. Here, we will consider the processes of plasma generation in magnetospheres of rotating magnetized neutron stars.

2. The magnetic field of neutron stars

Observations revealed that the energy lost by a rotating neutron star as radio pulsar is mainly spent on the formation of the flux of relativistic particles called the pulsar wind. Thus, it is precisely these relativistic particles that feed the entire Crab Nebula. The flux of such particles is about 10^{40} particles per second. Observations of the unique binary system consisting of two radio pulsars J0737-30039 A, B allow one to show how the pulsar wind from the more powerful pulsar compresses the magnetosphere of the star-companion several dozen-fold. The heating of the star-companion to the millisecond pulsar 1957+20 at orbital phases where the companion side turned toward the pulsar has also been observed.

However, for a long time the activity of a rotating neutron star was thought to be connected not with the wind emission but with the emission of the so-called magneto-dipole wave, an electromagnetic wave generated by the rotating magnetic dipole frozen in the star. The emission power of the magneto-dipole radiation, $dE/dt = 2\Omega^4 \mu^2 \sin^2 \chi / 3c^3$, was matched with the rotational energy losses of the neutron star. Here, $\Omega = 2\pi/P$ is the rotation frequency of the star, μ is its magnetic moment, and χ is the angle between the rotation axis and the magnetic dipole axis. The derived estimate of the surface magnetic field intensity $B = (P dP/dt_{-15})^{1/2} \times 10^{12}$ G exactly matched the expected values. (The notation dP/dt_{-15} means the rotational braking in units of 10^{-15} s s $^{-1}$).

The idea that the activity of rotating neutron stars is related to the presence of a strong magnetic field $B \simeq 10^{12}$ G was put forward by V L Ginzburg almost immediately after the discovery of radio pulsars. Indeed, assuming magnetic flux freezing, during the fast compression of the pre-supernova star by 10^5 times the magnetic field intensity increases by 10^{10} times. So, from the 100-G magnetic fields of ordinary stars we arrive at the above estimate of neutron star magnetic fields. Moreover, during the cooling of a neutron star after a supernova explosion, the magnetic field can be generated in the stellar core by the current of electrons carrying the heat flux. Observations of absorption cyclotron lines in the spectra of some X-ray sources also indicate a magnetic field strength of order 10^{12} G on the neutron star surface. The upper limit of the magnetic field intensity of a neutron star, 10^{18} G, is given by equating the magnetic field energy to the gravitational energy E_g of the neutron star.

As mentioned above, there are neutron stars belonging to a rather small but very active class, which demonstrate bright bursts of gamma- and X-ray emission and have significantly stronger magnetic fields than ordinary pulsars. Such stars rotate comparatively slowly with the periods $P \simeq 5-10$ s but undergo braking much faster, $dP/dt \simeq 10^{-10}-10^{-12}$ s s $^{-1}$. Their energy is caused by magnetic fields, not by rotation. The X-ray flux from such a star, $W_x \simeq 10^{35}-10^{36}$ erg s $^{-1}$, is much higher than the rotational energy losses defined as $\dot{E} = I\Omega d\Omega/dt$. The energy stored in the magnetic field, $\int (B^2/8\pi) dV$, is also larger than the rotational energy $I\Omega^2/2$ of the star. This suggests that the activity of such neutron stars is due to their magnetic fields and not the rotational energy, as is the case for ordinary radio pulsars. Such stars are thus termed magnetars.

The strong magnetic field in the neutron star magnetosphere provides conditions for plasma generation and the formation of a wind — the flux of relativistic electrons and positrons emitted by active stars.

3. Plasma generation

Effective particle creation begins at magnetic field intensities close to the intensity of a so-called critical magnetic field:

$$B_c = \frac{m^2 c^3}{e \hbar} = 4.4 \times 10^{13} \text{ G}.$$

Here, m and e are the mass and charge of an electron, c is the speed of light, and \hbar is the Planck constant. In such a magnetic field, the distance between the adjacent Landau levels is equal to the electron rest energy: $\hbar \omega_c = mc^2$. In such an electric field, the vacuum becomes unstable and electron–positron pair creation begins. The probability of one-photon pair creation in the magnetic field is given by

$$w = bB \sin \beta \exp \left(-\frac{8}{3Bk \sin \beta} \right), \quad B < 1,$$

where β is the angle between the photon wave vector and the direction of the magnetic field, k is the photon wave vector in units of the inverse electron Compton wavelength, the magnetic field intensity is measured in units of the critical magnetic field intensity, and b is a constant. Pair creation occurs above the threshold value of $k \sin \beta > 2$. It is seen that even in not very strong fields, $B < 10^{-2}$, typical in radio pulsars, photons with energy $k > 10^2$ effectively create pairs. In a strong magnetic field $B > 1$, pair creation probability is even higher:

$$w = bB \exp \left(-\frac{k^2 \sin^2 \beta}{2B} \right), \quad B > 1,$$

and electron–positron pairs form immediately after reaching the threshold.

Relativistic particles in the star magnetosphere rapidly lose transversal momentum due to synchrotron emission and move along the magnetic field. The magnetic field lines have a large curvature; the radius of curvature ρ near the surface changes from the stellar radius ($\simeq 10^6$ cm) at the equator up to about 10^8 cm near the pole. Particles moving along a curved trajectory emit so-called curvature photons with energies $k = 3\gamma^3/2\rho \simeq 10^4$, which is sufficient for subsequent pair creation. Here, γ is the Lorentz factor of a particle, and the radius of curvature is measured in units of the electron Compton wavelength \hbar/mc . Charged particles acquire significant energy (with Lorentz factors up to $\gamma \simeq 10^7$) by moving in the electric field E that appears in the rotating magnetosphere, $E \simeq \Omega R B/c$. The curvature photons, which initially propagate along the magnetic field lines, after passing the length l acquire the threshold angle β : $l/\rho = 2/k$, due to the field line curvature. In a strong magnetic field $B > 1$, the length l is the photon mean free path for pair creation. In a weak magnetic field $B < 1$, the mean free path is somewhat longer, $l = 8\rho/3kBA$, where A is a logarithmic factor ranging $A \simeq 10-15$. In this way, the electron–positron cascade in the neutron star magnetosphere is formed, as shown in Fig. 1.

In a weak magnetic field $B < 1$, the cascade strengthens due to particles being created at high Landau levels and

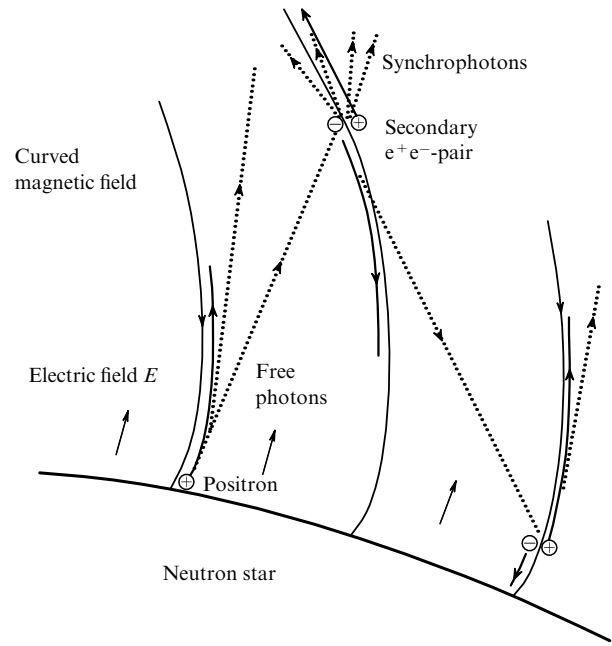


Figure 1. Schematic of the process of creation of an electron–positron pair in the magnetosphere of a neutron star near its surface. Particles are accelerated by the electric field, move along the magnetic field lines, and radiate curvature photons which, by crossing the magnetic field lines, produce electron–positron pairs. In a weak magnetic field $B < B_c$, particles created change to the ground Landau level and emit synchrophotons. In a strong magnetic field, particles are created on the ground or on the first Landau level.

emitting so-called synchrophotons during the transition to the ground level. These additional photons significantly increase the photon number. In a strong magnetic field $B > 1$, particle creation occurs either on the ground or on the first level, depending on the photon polarization.

Generally, radiation processes in a strong magnetic field greatly depend on photon polarization. Two polarizations are possible: (1) the longitudinal one, where the electric field of a photon lies in the plane (\mathbf{k}, \mathbf{B}) and has a nonzero projection onto the magnetic field, and (2) the transversal one, where the electric field is orthogonal to both the \mathbf{k} and \mathbf{B} vectors.

In a field $B > 1$, the decay of a transverse photon into two longitudinal ones, $k_\perp \rightarrow k_{1\parallel} + (k - k_1)_\parallel$, is possible. It had been thought earlier that these two facts, viz. the absence of synchrophotons and the radiation decay of a photon, suppress the plasma generation in a strong magnetic field of magnetar magnetosphere. This seemed to have been confirmed by observations—no magnetars were known to radiate radio emission. However, very low-frequency observations carried out at $\simeq 100$ MHz at the Pushchino Radio Astronomical Observatory of LPI have shown that there is an unusual radio emission from two magnetars [3, 4]. In addition, the anomalous X-ray pulsar (magnetar) XTE 1810-197 started to act as a powerful pulsar after the X-ray burst in 2003 [5]. In 2007, a magnetar emitting in the radio band was also discovered. This means that the generation of dense plasma in magnetar magnetospheres with a strong magnetic field $B > 1$ is also possible, as in pulsar magnetospheres with $B < 1$.

A plasma is called dense if the number density of particles exceeds some value called the Goldreich–Julian density n_{GJ} [6], which separates the vacuum magnetosphere of a neutron

star, where a nonstationary electromagnetic field is generated (magneto-dipole wave), and the stationary magnetosphere filled with plasma:

$$n_{\text{GJ}} = -\frac{B\Omega}{2\pi ce}.$$

This density near the neutron star surface, both in pulsars and magnetars, is of the order of 10^{12} cm^{-3} . Cascade creation of electrons and positrons in the magnetosphere of a radio pulsar leads to a number density much higher than n_{GJ} . The plasma particle multiplicity $\lambda = n/n_{\text{GJ}}$ reaches values of $\lambda = 10^4 - 10^5$ [7].

In magnetars with a strong magnetic field $B > 1$, the plasma particle multiplicity also turned out to be comparable with that in radio pulsars [8]. Although for $B > 1$ there is no second generation of particles, i.e., those created by synchrophotons, the number density of the first-generation particles created by the curvature photons is proportional to the magnetic field strength, $n \propto B$, which compensates for the lack of synchrophotons in a high magnetic field. The photon radiation decay leads to the 100% polarization of gamma quanta which become longitudinally polarized [8].

Thus, a strong magnetic field does not suppress plasma generation, as was thought before. The only factor suppressing plasma particle creation in magnetars is their slow rotation. On average, the rotation periods of magnetars is larger by two orders of magnitude than those of radio pulsars. Thus, the size of the polar cap where plasma is generated, $\simeq R(\Omega R/c)^{1/2}$, decreases by one order of magnitude. This increases the radius of curvature ρ of the magnetic field lines (at the dipole axis ρ is infinite). As a result, the energy range of electrons and positrons created becomes smaller. The minimum Lorentz factor $\gamma_{\text{min}} = \rho/R$ increases, while the maximum one $\gamma_{\text{max}} = 3\gamma_0^3/4\rho$ decreases. The energy $\gamma_0 mc^2$ equals the energy that particles acquire from a longitudinal electric field induced in the polar cap region. At $\gamma_{\text{max}} \simeq \gamma_{\text{min}}$, plasma generation in magnetars almost stops. This condition determines the range of parameters, the neutron star rotation period P and the magnetic field intensity B , where dense plasma generation is possible in magnetar magnetospheres:

$$P \left(\frac{B}{10^{12} \text{ G}} \right)^{-3/7} < 1 \text{ s}.$$

For radio pulsars, a similar boundary was determined in paper [7] (see also the book [9]): $P(B/10^{12} \text{ G})^{-8/15} < 1 \text{ s}$. The $(P, dP/dt)$ diagram for radio pulsars and magnetars, in which plasma generation boundaries are shown, is presented in Fig. 2. The magnetic field intensity and the rotation braking is related by the formula $B = (P dP/dt_{-15})^{1/2} \times 10^{12} \text{ G}$.

4. Conclusion

Observations of radio pulsars provide the possibility to explain how plasma generation occurs in magnetospheres of neutron stars. This possibility emerged during observations of a small group of so-called switch-off pulsars. These are pulsars in which radio emission temporarily disappears and then appears again. Such 'radio-quiet' and 'radio-loud' phases occurs at all times of observations. For example, careful observations of the pulsar PSR B1931+24, which is quiet for 20–25 days and then switches on for 5–10 days, showed that its rotation braking is significantly different during the quiet and loud phases [10]. The braking during

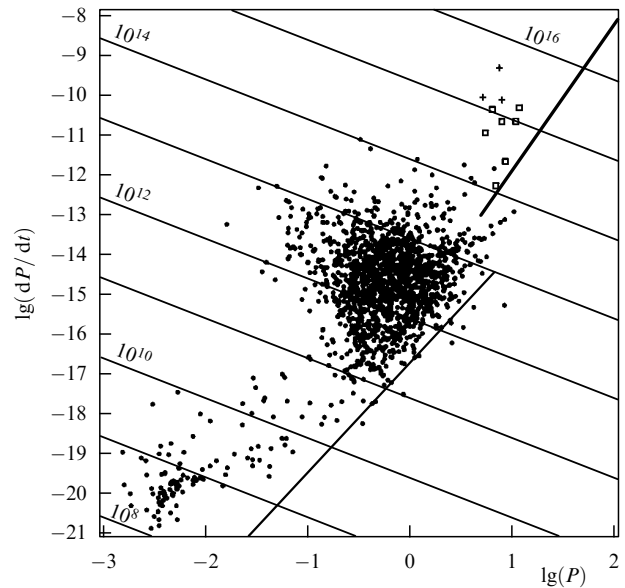


Figure 2. The $P - dP/dt$ diagram with boundary lines for effective pair creation. Circles are radio pulsars, while crosses and squares are magnetars. The thin line marks the plasma generation boundary for radio pulsars, $dP/dt \propto P^{11/4}$ [7], and the thick line is the plasma generation boundary for magnetars, $dP/dt \propto P^{11/3}$ [8].

the radio-loud phase is 1.5 times as effective as during the radio-quiet one. The explanation for this is that the radio emission is related to plasma generation, and the rotational energy of the neutron star is spent on the generation of the pulsar wind. The absence of radio emission, in turn, implies that no plasma is generated and the rotational energy is spent on the generation of magneto-dipole waves [11]. Hence, the energy losses are very different. Should one catch the moment of the switch-on, one could observe the development of cascade plasma generation, which should show up in the intensity and spectral range of the radio emission. At the switch-off moment, which lasts less than 10 s, one could observe the interaction of the magneto-dipole radiation with the pulsar wind. The point is that electromagnetic radiation propagates with the speed of light, faster than the wind, and when catching up with the wind the radiation starts interacting with it. The magnetic field of the radiation excites synchrotron radiation of relativistic particles in the wind. Measurements of the intensity and spectral range of such a radiation would allow the determination of the particle number density and particle energy spectrum in the wind.

In conclusion, we should note that the observations of neutron stars and the theory of the observed phenomena provide us with a fundamental understanding of the behavior of matter under extreme conditions, in particular, in super-strong magnetic fields.

References

1. Baade W, Zwicky F *Proc. Natl. Acad. Sci. USA* **20** 259 (1934)
2. Bell S J, Hewish A *Nature* **213** 1214 (1967)
3. Malofeev V M, Malov O I, Teplykh D A, in *Young Neutron Stars and Their Environments: Proc. of the 218th Symp. of the IAU, Sydney, Australia, 14–17 July 2003* (Eds F Camilo, B M Gaensler) (San Francisco, Calif.: Astron. Soc. of the Pacific, 2004) p. 261
4. Malofeev V M et al. *Astron. Zh.* **82** 273 (2005) [*Astron. Rep.* **49** 242 (2005)]

5. Camilo F et al. *Nature* **442** 892 (2006)
6. Goldreich P, Julian W H *Astrophys. J.* **157** 869 (1969)
7. Gurevich A V, Istomin Ya N *Zh. Eksp. Teor. Fiz.* **89** 3 (1985) [*Sov. Phys. JETP* **62** 1 (1985)]
8. Istomin Ya N, Sobyenin D N *Pis'ma Astron. Zh.* **33** 740 (2007) [*Astron. Lett.* **33** 660 (2007)]
9. Beskin V S, Gurevich A V, Istomin Ya N *Physics of the Pulsar Magnetosphere* (Cambridge: Cambridge Univ. Press, 1993)
10. Kramer M et al. *Science* **312** 549 (2006)
11. Gurevich A V, Istomin Ya N *Mon. Not. R. Astron. Soc.* **377** 1663 (2007)

PACS numbers: 63.20.kp, **63.22. – m**
DOI: 10.1070/PU2008v051n08ABEH006597

Multichannel propagation and scattering of phonons and photons in low-dimension nanostructures

Yu A Kosevich

1. Introduction

Recent major achievements in the research and development of technologically and functionally advanced materials have markedly increased research interest in the generation and propagation of coherent acoustic phonons in quasi-one-dimensional superstructures (including those with ‘acoustic nanocavities’ [1]), nanowires, and nanorods [2]. Of much importance in terms of potential applications is the study of phonon heat transfer in low-dimension systems — for example, through a solid–solid microcontact [3]. The search for technologically feasible materials for thermoelectric transducers lent very topical significance to the recent experimental finding that silicon nanowires with rough surfaces have a much lower thermal conductivity than their smooth-surface counterparts and bulk silicon [4–6]. Furthermore, the phonon contribution to the thermal conductivity of single-crystal silicon nanowires with a diameter of less than 50 nm approaches the limiting value found for amorphous silicon, something which current theories cannot explain [5]. Also, the molecular dynamics modeling of the thermal conductivity of diamond nanorods whose surfaces are coated with hydrogen with attached phenyl groups has shown that the thermal conductivity of nanorods is much less than that of bulk crystals [7].

This talk describes and discusses several examples of the so-called multichannel propagation and scattering of phonons and photons, two processes which can contribute to the phonon and photon characteristics, both dynamic and kinetic, of low-dimension systems.

The important thing about the multichannel propagation of phonons or photons is that there are several ‘parallel’ paths along which propagation is effected, between which both constructive and destructive interference can take place. Path-to-path interference occurring during multichannel propagation in a low-dimension system results in the transmission, reflection, and/or absorption coefficients generally having an asymmetric (non-Lorentzian) line shape as a function of the phonon (photon) frequency.

An asymmetric absorption line shape was first described by Fano [8] in his study of inelastic autoionization resonances in atoms and has been interpreted as due to discrete resonances interfering with the surrounding continuum of

‘background’ states. Although Fano type asymmetric absorption profiles have been discovered in many atomic systems (see, for example, Ref. [9]), they are not exclusive to them alone and have also been detected in doped semiconductor materials (the absorption [10] and Raman scattering [11] spectra taken from impurities), as well as in bulk intrinsic semiconductor GaAs and semiconductor superlattices [12, 13], and in quantum wells [14]. In the context of electron transport, conductivity as a function of applied voltage or gate voltage has been observed to exhibit asymmetric peaks in quantum dots with few electron levels [15, 16], crossed carbon nanotubes [17], and quantum wires with an attached ‘lateral’ quantum dot [18, 19]. The electron Fano effect in a quantum dot on one arm of an Aharonov–Bohm interferometer can interact with the Aharonov–Bohm effect [20, 21] and with Kondo correlations in the quantum dot [22]. For photons, the clearest manifestation of the Fano effect is the asymmetrically shaped line of the photon transmission coefficient through a two-dimensional system of local (plasmonic or optical-phonon) resonances [23, 24] or through a layer of a transparent material with a periodic arrangement (two-dimensional lattice) of holes [25, 26].

The phonon analogue of the Fano effect was first described in Ref. [27] and Ref. [28] independently. Reference [27] studied, in particular, the passage of a long acoustic wave (acoustic phonon) through a crystal two-dimensional (2D) defect with a complex structure. A peculiarity in considering such a 2D defect in crystal consisted in accounting for not only the interaction between the neighboring atomic layers closest to the defect but also the direct interaction of the lattice matrix rims through the defect monolayer. In an atomic model of the 2D defect this corresponds to the interaction between nonclosest neighbors. Reference [27] predicted that this essentially monolayer defect characterized by weak local force bondings of both nearest and more distant neighbors can fully reflect in a resonant manner acoustic phonons with wavelengths much larger than the physical thickness of the defect. From the viewpoint of the Fano effect interpretation, the reason for the anomalously strong reflection of an acoustic wave is the destructive interference between two phonon wave paths: through a local oscillator (or through the local bondings of the nearest neighbors) and through the local force bondings of the nonclosest neighbors, bypassing around the local oscillator. A further prediction of Ref. [27] was that a phonon undergoes total resonant absorption (total nonreflection and total nontransmission) at the boundary of a crystal 2D defect with a complex structure. As noted in Ref. [27], a normally incident, long-wave acoustic phonon cannot suffer anomalously strong resonant reflection (or absorption) by a laterally uniform layer of the material (see, for example, the well-known monograph [29]); this can only happen in the acoustics of composite materials. What a laterally uniform layer can only do is resonantly increase the phonon transmission coefficient under Fabry–Perot resonance conditions, thus demonstrating the phonon analogue of the resonant bleaching effect. The interaction of the matrix rims directly through the defect layer is equivalent to the lateral nonuniformity of a two-dimensional defect. Introducing this additional local interaction can also be regarded as effectively taking into account that impurities do not always fill the entire surface of a crystal 2D defect, i.e., impurity atoms can alternate in the plane of the defect with matrix atoms or, alternatively, there may be two or more types of impurities in a 2D defect (Fig. 1).

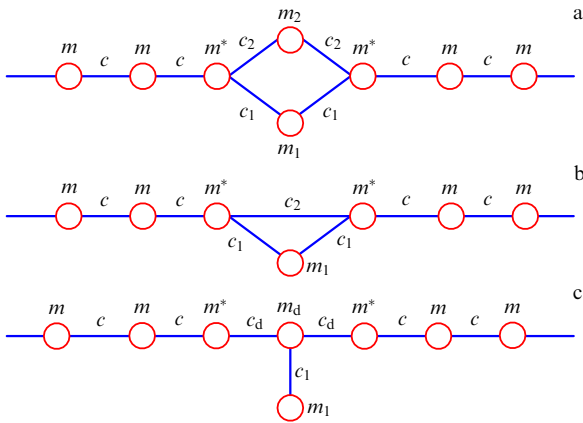


Figure 1. Three possible 1D lattice models describing the multichannel propagation of phonons through a lattice region containing a local defect.

Reference [28] drew an analogy between the scattering of electrons and the scattering of phonons and calculated numerically the phonon transmission coefficients with an asymmetric line shape for a quasi-one-dimensional multichannel waveguide consisting of a strip of oscillator chains connected in parallel. However, the oscillatory phenomena occurring in quasi-one-dimensional systems of oscillator chains were not generalized to the case of phonons propagating and undergoing a scattering in real 3D systems [28], such as that considered in Ref. [27] 2D defect of complex structure in a 3D crystal.

The later work [30] was the first to study experimentally the acoustic properties of a so-called ‘locally resonant’ material, a 3D lattice of rubber-coated steel balls embedded in a solid epoxy resin matrix. It was shown that at frequencies close to the natural frequency of a steel ball in a solid matrix, a ‘monolayer’ of such composite material is capable of essentially totally reflecting, in a resonant manner, the acoustic wave with a wavelength nearly two orders of magnitude larger than the physical thickness of the layer. It was shown, further, that the anomalously strong resonance reflection of an acoustic phonon from a composite layer is essentially unaffected by the irregular (not strictly 2D periodic) distribution of identical elastic-wave scatterers in the solid matrix. Both the material used and the resonance phenomenon observed in Ref. [30] can be given an immediate interpretation in terms of the model posed in Ref. [27] if the layer of steel balls in a solid matrix is regarded as a crystal 2D defect formed by ‘weakly coupled’ impurities, and the material of the matrix between ‘local resonators’ as a force bonding through the composite layer, bypassing around the resonators (Fig. 1a). It is significant that in both Ref. [27] and Ref. [30] the above effects were given a correct theoretical description and experimentally studied without using any analogies with the Fano effect. That acoustic phenomena in locally resonant materials can be interpreted in terms of a phonon analogue of the Fano effect was first brought to attention in Refs [31, 32] (note that, however, the analogy itself added nothing either to the theoretical description or to the experimental investigation of the acoustic phenomena in question). A two-dimensional system of thin-walled elastic hollow cylinders is, as shown in Ref. [33], another example where the peculiarities of the resonant propagation of acoustic waves are most naturally explained using an analogy with the Fano effect.

2. Multichannel scattering of acoustic phonons from a crystal two-dimensional defect

To macroscopically describe the scattering of a long-wave acoustic phonon from a crystal 2D defect requires that the form (and number) of boundary conditions for surface bulk strains ($\sigma_{zi} = \lambda_{zilm} u_{lm}$) and elastic displacements (u_i , $i = 1, 2, 3$) be specified on the surface of the defect ($z = 0$ plane). If the interface between two solids is sharp, then all that is needed is that these quantities be continuous (see Ref. [34]). In the general case, both the surface strains and elastic displacements exhibit discontinuities at the surface of a crystal 2D defect (see Ref. [35]). Denoting by N the number of types of atoms residing in the plane of the 2D defect, the simplest generalization of the multichannel propagation model posed in Ref. [27] reduces to the following dynamic equations on the surface of the defect:

$$\sigma_{zi}^{(1)} = \sum_{l=1}^N A_{ik}^{(l)} (u_k^{(ls)} - u_k^{(1)}) - \varrho \frac{\partial^2 u_i^{(1)}}{\partial t^2}, \quad (1)$$

$$\sigma_{zi}^{(2)} = \sum_{l=1}^N A_{ik}^{(l)} (u_k^{(2s)} - u_k^{(ls)}) + \varrho \frac{\partial^2 u_i^{(2)}}{\partial t^2}, \quad (2)$$

$$\rho_s^{(l)} \frac{\partial^2 u_i^{(ls)}}{\partial t^2} = A_{ik}^{(l)} (2u_k^{(ls)} - u_k^{(1)} - u_k^{(2)}), \quad (3)$$

where the z -axis is directed from medium 1 to medium 2; $u_i^{(1,2)}$ and $u_i^{(ls)}$ are the macroscopic (averaged) displacements of the matrix rims and surface atoms of the l type; the symmetric tensor $A_{ik}^{(l)}$ describes the interaction of the matrix rims with the surface atoms of the l type, while $\rho_s^{(l)}$ and ϱ are the surface densities of l type atoms and of atoms in the near-surface layers [the latter density should only be considered if it is large compared to the average ‘bulk’ density (see Fig. 4 below)]. For $N = 2$ and $\rho_s^{(2)} = 0$ (or $\rho_s^{(2)} \ll \rho_s^{(1)}$), equations (1)–(3) are reduced to those obtained in Ref. [27]:

$$\sigma_{zi}^{(1)} = A_{ik} (u_k^s - u_k^{(1)}) + B_{ik} (u_k^{(2)} - u_k^{(1)}) - \varrho \frac{\partial^2 u_i^{(1)}}{\partial t^2}, \quad (4)$$

$$\sigma_{zi}^{(2)} = A_{ik} (u_k^{(2)} - u_k^s) + B_{ik} (u_k^{(2)} - u_k^{(1)}) + \varrho \frac{\partial^2 u_i^{(2)}}{\partial t^2}, \quad (5)$$

$$\rho_s \frac{\partial^2 u_i^s}{\partial t^2} = A_{ik} (2u_k^s - u_k^{(1)} - u_k^{(2)}), \quad (6)$$

where $u_k^s = u_k^{(1s)}$, $\rho_s = \rho_s^{(1)}$, $A_{ik} = A_{ik}^{(1)}$, and the tensor $B_{ik} = (1/2) A_{ik}^{(2)}$ describes the ‘direct interaction’ between the matrix rims via the defect layer. When the normal to the surface of the 2D defect coincides with a symmetry axis of the crystal and when this is the only wave propagation direction of interest, then in the simplest case of interaction between only nearest neighboring atoms in the bulk of the crystal the 3D equations (1)–(3) and (4)–(6) can be reduced to 1D oscillator chain models (Figs 1a and 1b for the case of $N = 2$). Notice that in the latter of these models (Fig. 1b) the local force bondings near the defect correspond to the situation in which both the nearest and more distant neighbors interact. As can be seen by comparing Figs 1a and 1b, the latter force bondings can indeed effectively take into account force bondings through the matrix, bypassing around the defect atom.

The long-wave approximation allows a direct correspondence to be made between elasticity theory equations (4)–(6) (used, for example, to describe the interaction of a

z-propagating longitudinal phonon with a 2D defect) and the 1D lattice model of this 2D defect, presented in Fig. 1b:

$$\sigma_{zz} = \lambda_{zzzz} \frac{\partial u_z}{\partial z} \rightarrow \frac{c(u_{n+1} - u_n)}{a^2}, \quad (7)$$

and between all the parameters in both descriptions: $\lambda_{zzzz} \rightarrow c/a$, $A \rightarrow c_1/a^2$, $B \rightarrow c_2/a^2$, $\varrho \rightarrow m^*/a^2$, and $\rho_s \rightarrow m_1/a^2$, where a is the 1D lattice spacing. Below we will use the simple 1D lattice models of Fig. 1 as an example to describe the most interesting aspects of the multichannel propagation of phonons through a crystal 2D defect.

For a 2D defect coinciding with the $n = 0$ plane, the solution of the corresponding linear lattice equations for the planes $n \leq -2$ and $n \geq 2$ are assumed to be of the form

$$u_n = \exp(ikan - i\omega t) + r \exp(-ikan - i\omega t), \quad n \leq -2, \quad (8)$$

$$u_n = t \exp(ikan - i\omega t), \quad n \geq 2, \quad (9)$$

where ω and k are the frequency and wave number of the incident acoustic phonon, and r and t are the amplitude reflection and transmission coefficients, respectively. The reflection (R) and transmission (T) coefficients are respectively defined as $R = |r|^2$ and $T = |t|^2$. In the absence of dissipation, the condition to be satisfied is the conservation of energy for the incident acoustic phonon, $T + R = 1$, a condition we always check when carrying out calculations. Equations of motion for three planes — $n = -1$, $n = 0$, and $n = 1$ — are determined either by the long-wave approximation equations (1)–(3) [alternatively, (4)–(6)] or by the corresponding discrete lattice equations [due to the presence of correspondence (7) in the long-wave limit]. The phonon dispersion relation in the lattice under study is given by $\omega = \omega_{\max} \sin(ka/2)$ (where $\omega_{\max} = 2\sqrt{c/m}$), which is usual for a 1D monatomic model with the nearest neighbor interaction.

For the fault of direct interaction between the defect rims, $c_2 = 0$, the presence of a weakly coupled defect, for example, with $c_1 = 0.07c$ and $m_1 = m^* = m$, brings about the resonant passage of the phonon through the system at $\omega = \omega_0 \approx \sqrt{2c_1/m_1} \ll \omega_{\max}$ against the background of its transmission decreasing as a whole with increasing frequency [36] (Fig. 2a). This transmission resonance is analogous to the acoustic Fabry–Perot resonance at a monolayer of a ‘soft’ laterally uniform material embedded in a more ‘rigid’ medium. Allowing for a second phonon propagation channel, one with $c_2 \geq c_1$ (and with or without a matrix atom with $m_2 = m$ or $m_2 = 0$, see Fig. 1a), results in our obtaining, instead of the total resonance transmission of the phonon, its total resonance reflection at the same frequency $\omega_0 \approx \sqrt{2c_1/m_1}$ (Fig. 2c, corresponding to the model of Fig. 1a with $c_2 = 0.9c$, $c_1 = 0.07c$, and $m_2 = m_1 = m^* = m$). This effect, first described in Ref. [27], provides the clearest evidence for the influence of an additional channel on the propagation and scattering of phonons in low-dimension multichannel systems and nanostructures. Because for a weakly coupled defect the resonance frequency is low, $\sqrt{2c_1/m_1} \ll \omega_{\max} = 2\sqrt{c/m}$, the wavelength of a totally reflected phonon is much larger than the physical width $d \approx 2a$ of the nanodefekt.

As noted earlier and as is clear from the properties of the systems discussed, a phonon incident normal to a 2D defect can only suffer total reflection from a laterally nonuniform and ‘locally resonant’ composite layer. For an intermediately

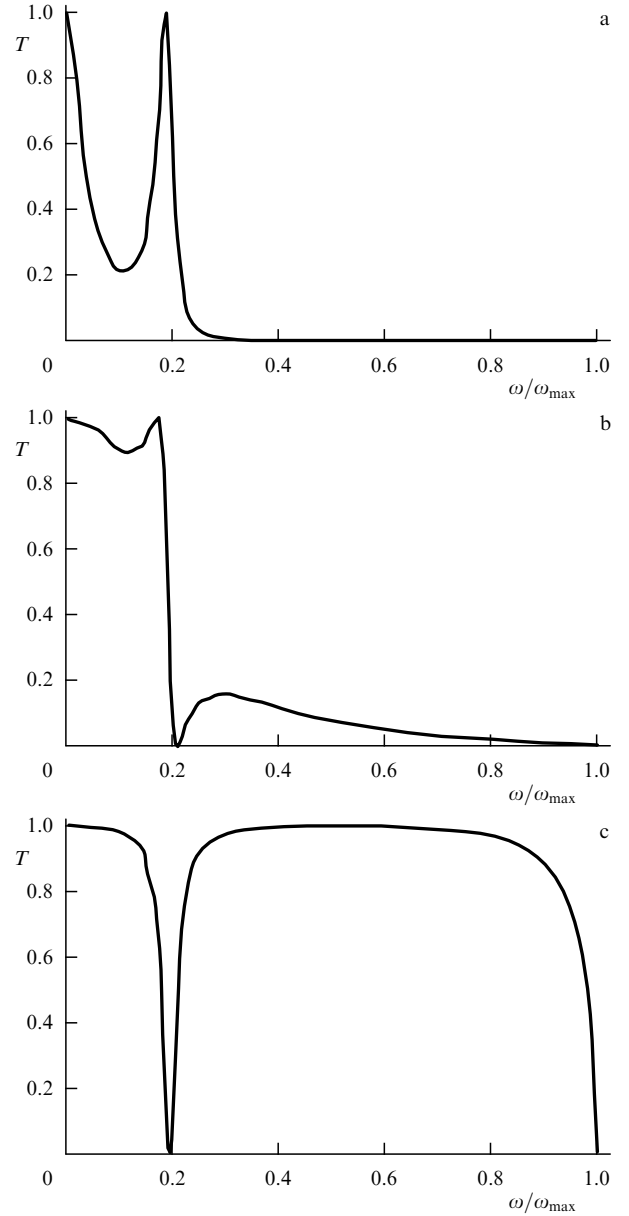


Figure 2. Energy transmission coefficients as functions of the normalized frequency ω/ω_{\max} for phonons passing through a lattice 2D defect. The one-dimensional projection of the defect corresponds to the model shown in Fig. 1a with $m_1 = m^* = m$ and (a) $c_1 = 0.07c$, $c_2 = 0$, (b) $c_2 = 4c_1 = 0.28c$, $m_2 = 0$, and (c) $c_1 = 0.07c$, $c_2 = 0.9c$, $m_2 = m$.

strong force bonding relevant to the direct interaction between lattice matrix rims, the frequency dependence of the transmission coefficient acquires asymmetric form, as is characteristic of the Fano effect (Fig. 2b, corresponding to the Fig. 1a model with $c_2 = 4c_1 = 0.28c$, $m_1 = m^* = m$, $m_2 = 0$ or to the Fig. 1b model with $c_2 = 2c_1 = 0.14c$, $m_1 = m^* = m$). In this case, the phonon transmission coefficient takes both zero and unity values at frequencies close to ω_0 .

The same features are seen in the passage of phonons through a nanodefekt in a quasi-one-dimensional waveguide with a ‘lateral’ oscillator (or a chain thereof) attached to it to serve as a ‘phonon lead’ (Fig. 1c). For a given weak force bonding in the phonon lead, $c_1 \ll c$, the transmission coefficient for a given weak force of the ‘longitudinal bonding’ of the defect, $c_d \ll c$, has one or several *transmission resonances*

of the Fabry–Perot type. For a relatively strong longitudinal bonding of the defect, $c_d \approx c \gg c_1$, the transmission coefficient has one or several *reflection resonances* in the low frequency range against the background of almost total transmission for the rest of the frequencies. In particular, if a phonon lead with one, two, or three series-connected, identical, weakly coupled links for each of which $m_l = m$ and $c_l \ll c$ is attached to one site of the 1D lattice with $m_d = m$ and $c_d = c$, then the propagation of a long-wave phonon through such a defect is characterized by the presence of one, two, or three resonance frequencies, respectively, at which total reflection occurs (see Fig. 3 for the case of $c_1 = 0.1c$). For each such resonance, the second phonon propagation channel, whose destructive interference with the channel along the 1D crystal results in the complete suppression of

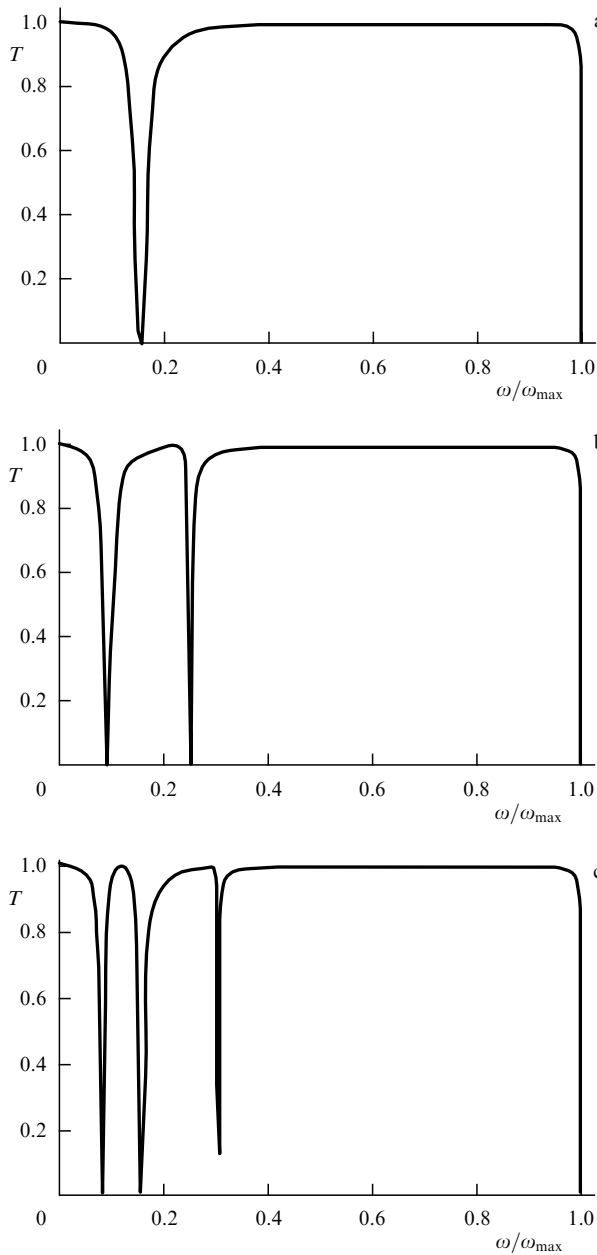


Figure 3. Energy transmission coefficients versus frequency for phonons passing through a 1D waveguide containing a lateral chain depicted in Fig. 1c with one (a), two (b), and three (c) identical links for the case of $m_d = m_l = m$, $c_d = c$, and $c_1 = 0.1c$.

transmission, is one of the natural vibrational modes of the phonon lead, the total number of the modes being determined by the number of links in the lead. The 1D crystal model with phonons lead will be used in what follows to simulate the phonon thermal conductivity of nanowires with dynamically rough surfaces.

Multiple phonon transmission zeros are also found in a 1D lattice (or a crystal 2D defect) with several parallel propagation channels similar to those in Fig. 1a. In the general case, N transmission channels can produce $N - 1$ total reflection resonances.

The large mass m^* of near-surface atoms and the correspondingly large near-surface density ϱ in Eqns (1)–(6) are further crucial factors for the resonant transmission of a phonon through 2D defects of the crystal whose 1D lattice models are shown in Fig. 1 [27]. In particular, the simplest 1D model depicted in Fig. 1b accounts for the presence of one or two resonance transmission peaks through two or three layers of strongly bounded ‘heavy’ impurity atoms, when $c_1 = 0$, $c_2 = c$, $m^* = 5m$ and $c_1 = c$, $c_2 = 0$, $m^* = m_1 = 5m$, respectively (Figs 4a and b). In other words, N strongly coupled dense layers produce $N - 1$ Fabry–Perot type phonon transmission resonances with a characteristic frequency (or interfrequency interval) $\omega_{hl} \approx \sqrt{2c/m^*}$ [unlike N weakly coupled layers leading to N phonon transmission resonances of the Fabry–Perot type (Fig. 2a)]. As far as electron transport in the strongly coupled 1D lattice model is concerned, the reader is referred to papers [37, 38] for a discussion of the resonance transparency of a pair of equal-energy sites (dimer) and how this transparency influences the delocalization of electron states in random dimer lattices and, in particular, in conducting polymers.

An additional resonance in transmission through the vibrating ‘dimer’ of strongly coupled dense layers can produce a ‘double’ transmission resonance (double Fano type resonance), in which the natural frequencies of two strongly coupled dense outer layers coincide with those of a weakly coupled inner layer (Fig. 1b). In this case, a narrow reflection resonance (a transmission minimum) is observed against a background of transmission resonance (Fig. 4c). However, a particularly pronounced effect can be observed in the case of natural vibrations undergoing finite dissipation under double-resonance conditions; this is the total surface absorption of an incident phonon by a lattice 2D defect [27], an effect in which the transmission and reflection coefficients simultaneously tend to zero and the surface absorption $A_s = 1 - T - R$ approaches unity (Fig. 4d). Phenomenologically, the dissipation of vibrations can be introduced through the imaginary parts of the constants of local force bondings c_1 and c_2 , which are assumed to be proportional to the frequency and small compared to the real parts of the corresponding force constants. For total surface absorption, $A_s \approx 1$, the following conditions must be satisfied [27]:

$$\omega_0 = \sqrt{\frac{2c_1 + c_1^2/c_2}{m_1}} = \sqrt{\frac{c_1 + 2c_2}{m^*}}, \quad (10)$$

$$\frac{m^*}{m_1} = \frac{c_2}{c_1}, \quad \text{Im}(c_1 + 2c_2) = 2c \frac{\omega_0}{\omega_{\max}}. \quad (11)$$

Figure 4d displays the transmission, reflection, and surface absorption coefficients which are calculated for the following parameters of a 2D defect as modelled by Fig. 1b: $c_1 = c(0.2 - i0.0165\omega/\omega_{\max})$, $c_2 = c(1 - i\omega/\omega_{\max})$, $m^* = 5m$,

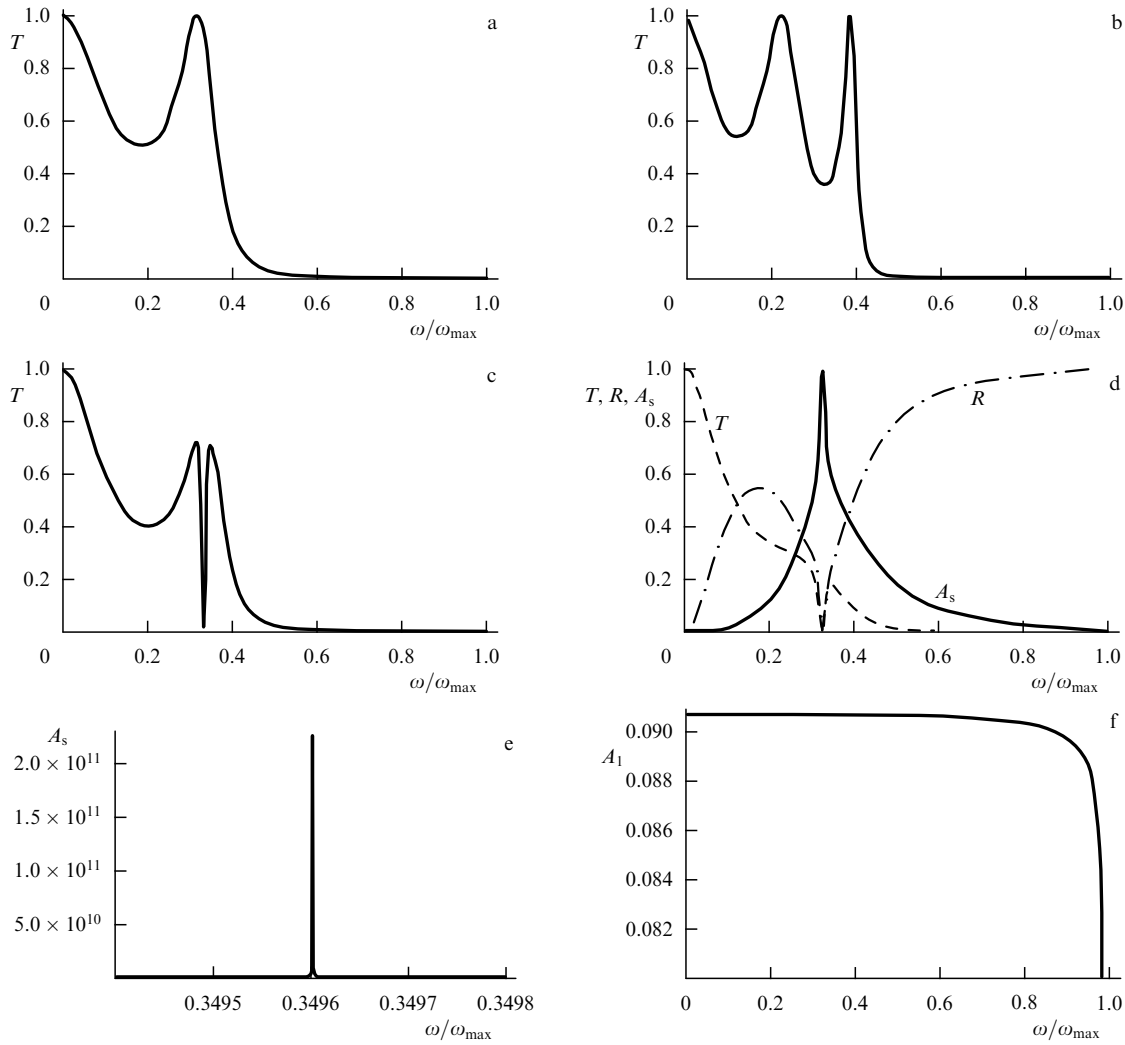


Figure 4. Energy transmission coefficients versus frequency for phonons passing through a 2D lattice defect containing two (a), (c)–(e) and three (b) high-density atomic layers and corresponding to the one-dimensional model of Fig. 1b with (a) $m^* = 5m$, $c_1 = 0$, $c_2 = c$, (b) $m^* = m_1 = 5m$, $c_1 = c$, $c_2 = 0$, and (c) $c_1 = 0.2c$, $c_2 = c$, $m^* = 5m$, $m_1 = m$. (d) Energy transmission (T), reflection (R), and surface absorption ($A_s = 1 - T - R$) coefficients as functions of frequency for a 2D defect with $c_1 = c(0.2 - i0.0165\omega/\omega_{\max})$, $c_2 = c(1 - i\omega/\omega_{\max})$, $m^* = 5m$, and $m_1 = m$. (e) Energy amplification coefficient $A_s = T + R - 1$ as a function of frequency for a 2D defect with $c_1 = c(0.2 + i0.0168\omega/\omega_{\max})$, $c_2 = c(1 + i0.92850\omega/\omega_{\max})$, $m^* = 5m$, and $m_1 = 0.88m$. (f) Energy loss coefficient $A_l = 1 - R_l - T_l$ as a function of frequency for a 1D waveguide for reflection from a single phonon lead (Fig. 1c) with an effective mass (18) and the dimensionless coupling parameter $f = c_1/c = m_l/m = 0.1$.

$m_1 = m$, and which agree with the analytical prediction following from formulas (10) and (11).

Based on the effect of the total absorption of an acoustic phonon by a double resonance layer—an effect similar to the total absorption of a flux of photons by resonant atoms in optics—it is, in principle, possible to build a phonon laser working by amplifying a radiation-stimulated (with $|A_s| \gg 1$) phonon field propagating through a preliminary excited double resonance layer. (This amplification mechanism is different from the mechanism studied in Ref. [39], by which acoustic phonons are resonantly emitted from a weakly coupled semiconductor superlattice.)

Because stimulated radiation corresponds to the case of a ‘negatively absorbed’ phonon field, values of $|A_s| \gg 1$ can be reached by changing the sign of the imaginary parts of the force bonding constants c_1 and c_2 . Figure 4e exhibits the resonant value of energy amplification coefficient $A_s \sim 2 \times 10^{11}$, which is achieved at a double resonance layer (Fig. 1b model) with $c_1 = c(0.2 + i0.0168\omega/\omega_{\max})$, $c_2 = c(1 + i0.92850\omega/\omega_{\max})$, $m^* = 5m$, and $m_1 = 0.88m$. With this

large numerical value of the amplification coefficient, it is hopeful that a system of appropriate double vibrational layers will indeed be able to produce a strengthened phonon field in the sample.

3. Acoustic phonon scattering in a quasi-one-dimensional waveguide with surface phonon leads

This section will discuss a phonon scattering model by a system of surface phonon leads in a quasi-one-dimensional waveguide. In this model it is assumed that an (infinitely) long oscillator chain with a small dimensionless coupling coefficient $f \ll 1$ is attached to each atom in the 1D crystal (phonon waveguide), when $c_1 = fc$, $m_1 = fm$ (Fig. 5). Phonon propagating along the waveguide excites vibrations in a lead, which propagate along the lead and, most importantly, do not return to the waveguide as a coherent phonon. We will apply this model to describe phonon scattering by a ‘dynamic roughness’ on the surface of a quasi-one-dimen-

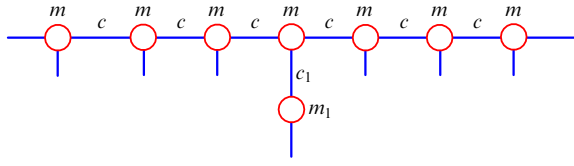


Figure 5. Schematic of the one-dimensional waveguide with identical phonon leads attached to each site as an extension of the one-dimensional model of Fig. 1c with a single lead defect.

sional waveguide and how this scattering influences the phonon thermal conductivity of nanowires. In the layer of a dynamic roughness there occur random intersections and contacts between different phonon leads, which, in turn, results in a phonon suffering random scatterings in its travel along a lead and, correspondingly, not returning to the waveguide as a coherent wave (in-phase with the generating phonon in the waveguide). In the dynamic lattice model, a dynamic roughness can be described by a random arrangement of vacancies and vacancy clusters in the lattice layer of atoms, which surrounds the waveguide. The dimensionless coupling coefficient $f < 1$, a characteristic of dynamic coupling between the ‘single-crystal’ waveguide and the disordered waveguide in the surface layer, can be related to the dimensionless vacancy ‘filling factor’ in this layer.

As seen from Fig. 3, with increasing N (the number of links in a lead), the minimum total reflection frequency decreases (as $\omega_N \sim \sqrt{c_1/m_1} \pi/N$ for $N \gg 1$), the total reflection frequencies condensing in the low-frequency region. For $N \gg 1$, this is equivalent to the formation of an effective quasigap in the low-frequency vibrational spectrum of such a quasi-one-dimensional system: in the quasigap, vibrations become strongly damped and their passage through a finite length system is hindered, correspondingly decreasing the phonon thermal conductivity of the system.

We assume that displacements in the n -th phonon lead take the form of a wave outgoing from the waveguide and carrying its vibrational energy away:

$$u_{m,n} = A_{1,n} \exp[-i\omega t + ik_{\perp}a(m-1)], \quad (12)$$

where $m = 1, 2, \dots$ are the atomic numbers in the link counted in the direction away from the waveguide, and k_{\perp} is the wave number along the waveguide, which is related to the wave frequency by the relationship $\omega = 2\sqrt{c_1/m_1} \sin(k_{\perp}a/2)$. In the low-frequency and long-wave limit $k_{\perp}a \ll 1$, we find $k_{\perp}a \approx \omega\sqrt{m_1/c_1}$. Using formula (12), we obtain

$$\begin{aligned} & \left[m\omega^2 - 4c \sin\left(\frac{k_{\parallel}a}{2}\right)^2 \right] \left[m_1\omega^2 - c_1 + c_1(\exp(ik_{\perp}a) - 1) \right] \\ & = c_1 \left[m_1\omega^2 + c_1(\exp(ik_{\perp}a) - 1) \right] \end{aligned} \quad (13)$$

for the dispersion of a phonon with the wave number k_{\parallel} along a quasi-one-dimensional waveguide with surface leads. From this, passing to the low-frequency (long-wave) limit $(k_{\parallel}, k_{\perp})a \ll 1$, when $k_{\perp}a \approx \omega\sqrt{m_1/c_1}$, we arrive at the equation for the complex wave number k_{\parallel} of a damping phonon:

$$k_{\parallel}^2 a^2 = \omega^2 \frac{m+m_1}{c} + i\omega \frac{\sqrt{m_1 c_1}}{c}. \quad (14)$$

This equation implies that in the frequency range $\omega \gg \omega^* \equiv \sqrt{m_1 c_1}/(m+m_1)$ phonons are weakly damped (the imaginary part of the phonon wave vector is small and frequency-independent) and propagate ballistically:

$$k_{\parallel} a = \omega \sqrt{\frac{m+m_1}{c}} + \frac{i}{2} \sqrt{\frac{m_1 c_1}{(m+m_1)c}}. \quad (15)$$

In the low-frequency limit, $\omega \ll \omega^*$, phonons are strongly damped:

$$k_{\parallel} a = \frac{1+i}{\sqrt{2}} \sqrt{\omega} \frac{(m_1 c_1)^{1/4}}{\sqrt{c}}, \quad (16)$$

and propagate diffusively in accordance with the equation $i\omega = D_{\text{ph}} k_{\parallel}^2$ comprising the diffusion coefficient

$$D_{\text{ph}} = \frac{ca^2}{\sqrt{m_1 c_1}} = V_{\text{ph}} l_{\text{ph}}, \quad (17)$$

where $V_{\text{ph}} = a\sqrt{c/m}$ is the velocity of long-wave phonons, and $l_{\text{ph}} = a\sqrt{mc/m_1 c_1} \equiv a/f$ is the phonon mean free path. This latter is also defined as half the inverse imaginary part of the ballistic phonon wave vector as given by formula (15). In conformity with the definition of the absorption coefficient of an acoustic phonon [34], twice the imaginary part of the wave vector defines the absorption coefficient of phonon energy. Consideration of the energy loss coefficient $A_1 = 1 - R_1 - T_1$ of a phonon on a single phonon lead yields a similar estimate for the phonon mean free path. The presence of a phonon lead is tantamount to the renormalization of the mass m_1 in a waveguide with a single lateral oscillator (Fig. 1c). In this case, the mass m_1 is replaced by a complex effective mass

$$\begin{aligned} m_1^{\text{eff}} &= m_1 + \frac{c_1}{\omega^2} [\exp(ik_{\perp}a) - 1] \\ &\equiv f \left[m + \frac{c}{\omega^2} (\exp(ik_{\perp}a) - 1) \right]. \end{aligned} \quad (18)$$

Figure 4f presents the frequency dependence of the energy loss coefficient A_1 in a one-dimensional waveguide for reflection from a single ‘lateral defect’ with the effective mass (18) for the case of $f = 0.1$. It is seen that $A_1 \approx f$ over a very wide frequency range, including low frequencies. Therefore, if such scatterers are arranged in the waveguide with a spatial period a , the mean free path of a phonon in respect to energy is estimated to be $l_{\text{ph}} \approx a/f$, which is in line with formula (17).

Let us now estimate the dimensionless dynamic coupling coefficient $f \ll 1$ between a phonon lead and a waveguide. For a rod with a circular or rectangular cross section, this parameter can be estimated as the ratio of the number of force atomic bonds in the rough surface layer to that in the undistorted portion of the waveguide, i.e., as $f \sim \delta/D$, where $\delta \sim \sqrt{h^2}$ is the root-mean-square roughness height, and D is the nanowire diameter. The phonon mean free path is then estimated to be

$$l_{\text{ph}} \approx \frac{a}{f} \sim \frac{a}{\delta} D \ll D. \quad (19)$$

From formulas (17) and (19) we obtain the following estimate for the phonon thermal conductivity κ_{ph} of a

nanowire with a dynamically rough surface:

$$\kappa_{\text{ph}} \sim C_{\text{ph}} D_{\text{ph}} \sim C_{\text{ph}} V_{\text{ph}} \frac{a}{\delta} D, \quad (20)$$

where C_{ph} is the phonon specific heat.

Thus, phonon scattering from dynamic roughnesses in nanowires decreases the phonon mean free path (and hence the phonon contribution to thermal conductivity) as the parameter a/δ decreases. Because $a \approx 0.54$ nm in silicon and the root-mean-square roughness height varied in the range 1–5 nm [5], the parameter δ/a falls within the range 2–10. This ratio of the phonon mean free paths (and thermal conductivity) in smooth and rough surface nanowires (with $\delta \sim a$ and $\delta \gg a$, respectively) is consistent with the experimental value of 5–8 for the corresponding factor [5].

What seems contradictory about estimate (19) is that because of scattering from the surface the phonon mean free path turns out to be less than the diameter of the sample: it is usually considered that $l_{\text{ph}} = D$ is the minimum mean free path for such scattering (see, for example, Refs [5, 40]). However, this contradiction is resolved if it is remembered that estimate (19) refers primarily to the phonons traveling along the axis of the waveguide, whereas the restriction $l_{\text{ph}} = D$ refers to those traveling at arbitrary (including large) angles to the axis. But it is exactly the axially traveling longitudinal phonons that make the most contribution to the nanowire thermal conductivity due to the largest projection of the group velocity $V_{\text{ph}z}$ on the axis of the quasi-one-dimensional sample [see formula (20)]. Applying estimate (19) primarily to the axially propagating phonons also removes the ‘quasi-one-dimensionality’ restriction on nanowire phonons, i.e., the requirement $k_{\text{ph}} D < 1$ (where k_{ph} is the wave number of a thermal phonon) which is met only at very low temperatures, even in nanowires with an average diameter of 100 nm ($\approx 200a$) [5]. On the other hand, when the parameter a/δ becomes very small with increasing root-mean-square roughness height, it should be remembered that the phonon mean free path (19) cannot be less than half the phonon wavelength $\lambda_{\text{ph}}/2$ (see Ref. [41]). Therefore, in nanowires with small enough diameters and rough surfaces the phonon mean free path can tend to $\lambda_{\text{ph}}/2$, while the phonon thermal conductivity to the lower limit of thermal conductivity for an amorphous solid. The fact that the thermal conductivity of nanowires made of *single-crystal silicon* tends to the limiting value of the thermal conductivity of *amorphous silicon* as the diameter of a rough surface nanowire decreases was also discovered (but not explained) in Ref. [5].

To summarize, the proposed mechanism of nonresonant phonon scattering from surface phonon leads that model the dynamic surface roughness of a phonon waveguide allowed us to explain, qualitatively and in part quantitatively, the significantly (almost by an order of magnitude) reduced thermal conductivity of rough-surface, compared to smooth-surface, nanowires, as well as to suggest the reason why nanowires of single-crystal materials achieve the lower limit of thermal conductivity found in an amorphous solid. The important point here is that the ‘parallel dynamic connection’ of an ideal heat conductor (crystalline phonon waveguide) with a poor heat conductor (disordered surface lattice layer) leads to a marked reduction in the thermal conductivity of the composite as a whole—unlike the electric conductivity of parallel-connected ideal (for example, superconducting) and resistive electric conductors.

4. Multichannel photon scattering from two-dimensional nanostructures

The idea of multichannel propagation may find another application to the scattering of photons from two-dimensional systems. Similarly to acoustic phonons, an additional propagation channel can result in a photon being totally reflected from a two-dimensional system with a physical thickness much smaller than the incident wavelength. Reference [23] gives examples of various anisotropic and/or gyrotropic 2D systems that scatter a photon such that it undergoes total reflection or total polarization conversion. The simplest system of this type is a thin layer of a polar, cubic GaAs type semiconductor whose characteristic frequency dispersion of the dielectric constant, $\varepsilon_{ik} = \varepsilon\delta_{ik}$, is due to optical phonons [42]:

$$\varepsilon = \varepsilon_{\infty} + \frac{\varepsilon_0 - \varepsilon_{\infty}}{1 - \omega^2/\omega_{\text{TO}}^2 - i\Gamma\omega/\omega_{\text{TO}}^2}, \quad (21)$$

where ε_0 and $\varepsilon_{\infty} < \varepsilon_0$ are the static and optical dielectric constants, and ω_{TO} and Γ are the frequency and the attenuation constant of a long-wave transverse optical phonon. It is a simple matter to see [see formulas (22) and (23) and Fig. 6] that close to the frequency ω_{TO} , at which $\varepsilon \rightarrow \infty$, a resonant increase occurs in the reflection coefficient from a thin layer at the interface between two media (including the case in which such a layer resides in a vacuum). In this case, the reflection curve is generally asymmetric as a function of frequency (see Fig. 6). The increase in the reflection coefficient at resonance is greater, the higher the quality factor [which is described by the parameter $\omega_{\text{TO}}/\Gamma$ in formula (21)] of the optical phonon is. However, if the thin semiconductor layer is at the interface of two identical media (for example, in a vacuum), then for $\varepsilon(\omega) = 1$, $\omega > \omega_{\text{TO}}$ the photon undergoes total transmission through the layer. The asymmetric shape of the transmission coefficient through a thin layer of a polar semiconductor can be related to the interference of two photon paths: through a resonance with an optical phonon, and through the surrounding medium with dielectric constant ε_{∞} , i.e., with the Fano effect for photons.

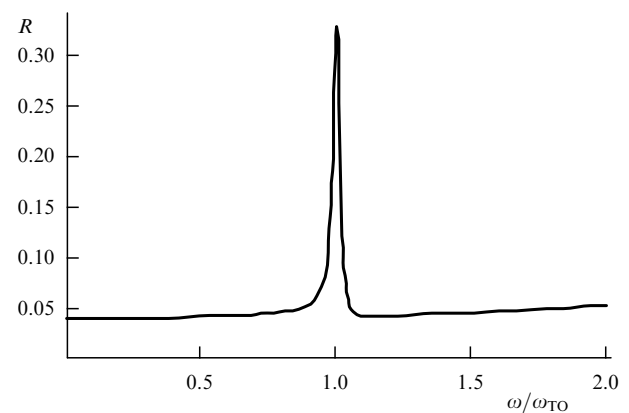


Figure 6. Energy reflection coefficient as a function of normalized frequency for a photon incident on a 100-nm-thick layer of polar GaAs semiconductor at the vacuum–glass interface; ω_{TO} is the frequency of a transverse optical phonon. The remaining layer parameters are given in the text.

Another photon analogue of the Fano effect is presented by the interaction of photons with a two-dimensional metal – dielectric type nanostructure consisting, for example, of single or double strips of 2D electron gas on a substrate of a GaAs type semiconductor [43], or of resonant metallic elements like split double [44, 45] or single [46] ring cavities on glass substrates. Resonantly enhanced photon reflection from such *structured* (laterally nonuniform) 2D electronic systems is observed in the far infrared [43, 44] and in the optical range with $\nu \approx 100$ THz [45, 46]. Common to all of these structured two-dimensional electronic systems (STDESs) is the fact that photons interact with local electronic nanostructures (LENs) located at a certain concentration on a transparent substrate and exhibiting local electron – plasmon resonances. This suggests that a resonant reflection enhancement can be related to the destructive interference of two photon paths: through a local electron – plasmon resonance, and through the transparent substrate surrounding the resonator.

Macroscopically, the interaction of a photon with a 2D system is described in the general case in terms of the effective dynamic conductivity $\sigma_{\alpha\beta}(\omega)$, $\alpha, \beta = 1, 2$ of the 2D system, which relates the surface (dynamic) current to the electric field component tangent to the surface (see, for example, Refs [23, 47]). For a photon normally incident from medium 1 to medium 2 with respective refraction indices n_1 and n_2 , the following expressions can be obtained for the amplitude coefficients of reflection ($r^{(x,y)}$) and transmission ($t^{(x,y)}$) for the photon electric field polarized along the x - or y -axis, respectively, in the plane of the 2D system:

$$r^{(x,y)} = \frac{n_1 - n_2 - (4\pi/c) \sigma_{xx,yy} + \frac{[(4\pi/c) \sigma_{xy}]^2}{n_1 + n_2 + (4\pi/c) \sigma_{yy,xx}}}{n_1 + n_2 + (4\pi/c) \sigma_{xx,yy} - \frac{[(4\pi/c) \sigma_{xy}]^2}{n_1 + n_2 + (4\pi/c) \sigma_{yy,xx}}},$$

$$t^{(x,y)} = 1 + r^{(x,y)}, \quad (22)$$

where c is the speed of light in vacuum. Equation (22) also describes the possible anisotropy and/or gyrotropy of the 2D electronic system, which in the general case are introduced through the different diagonal (σ_{xx} and σ_{yy}) and the off-diagonal (σ_{xy}) components of the 2D conductivity tensor $\sigma_{\alpha\beta}$. The dynamic 2D conductivity tensor $\sigma_{\alpha\beta}(\omega)$ can, in the general case, be related to the ‘excess’ local dielectric susceptibility tensors $(\epsilon_{\alpha\beta}(\omega) - \epsilon^{(1)}\delta_{\alpha\beta})/4\pi$ in the thin layer of thickness d and average dielectric susceptibility tensor at the interface of two (isotropic) media 1 and 2, $(\bar{\epsilon} - \epsilon^{(1)})\delta_{\alpha\beta}/4\pi$, $\bar{\epsilon} = (\epsilon^{(1)} + \epsilon^{(2)})/2$, with respect to the susceptibility of medium 1 (with lower dielectric constant, $\epsilon^{(1)} \leq \epsilon^{(2)}$):

$$4\pi\sigma_{\alpha\beta} = -i\omega d \left[\epsilon_{\alpha\beta} + \left(\frac{\epsilon^{(2)}}{2} - \frac{3}{2} \epsilon^{(1)} \right) \delta_{\alpha\beta} \right], \quad (23)$$

where it is assumed that $\omega d/c \ll 1$.

Figure 6 depicts the frequency dependence of the energy reflection coefficient of a photon (incident normally from a vacuum) from a GaAs layer of thickness $d = 100$ nm located at a vacuum – glass interface. The calculations performed used formulas (21)–(23) with the following values of GaAs parameters: $\epsilon_0 = 12.9$, $\epsilon_\infty = 10.9$, $\omega_{TO} = 2\pi \times 8$ THz, $\Gamma = 0.77 \times 10^{12} \text{ s}^{-1}$, and with $\epsilon^{(2)} = 2.25$ for glass. As seen from the figure, at resonance with a transverse optical phonon

a large increase from 4% to 33% indeed occurs in the reflection coefficient of a T-photon from a nano-thickness layer of a polar semiconductor (the photon wavelength in vacuum is 375 times the film thickness!). For a photon reflected from the same GaAs layer in a vacuum, the energy reflection coefficient varies from essentially zero out of resonance to 28% at resonance ($\omega = \omega_{TO}$). It should be noted that calculations based on formulas (21)–(23) agree to a high accuracy with those using expressions for R and T known from the optics of layered media (see Ref. [29]), with the same GaAs layer parameters.

For an STDES at the interface of two media, in the presence of a perpendicular magnetic field B , the following expressions can be obtained for the components of the 2D conductivity tensor [23]:

$$\sigma_{xx,yy} = i \left[\frac{n_s e^2 \omega}{m_{xx,yy}^* (\omega^2 - \omega_c^{*2})} - \frac{1}{4\pi} (\bar{\epsilon} - \epsilon^{(1)}) \omega d^* \right], \quad (24)$$

$$\sigma_{xy} = -\sigma_{yx} = \frac{n_s e^2 \omega_c^*}{\sqrt{m_{xx}^* m_{yy}^*} (\omega^2 - \omega_c^{*2})}, \quad (25)$$

$$m_{xx,yy}^* = m^* \left[1 - \frac{\omega_{0x,y}^2}{\omega^2} + \frac{i\gamma}{\omega} \right], \quad (26)$$

$$\omega_{0x,y}^2 = \frac{2\pi^2 \tilde{n}_s e^2}{\bar{e} m^* W_{x,y}}, \quad n_s = n_{ds} N_d = n_{ds} \tilde{n}_s W_x W_y, \quad (27)$$

$$\omega_c^* = \frac{eB}{c \sqrt{m_{xx}^* m_{yy}^*}}, \quad (28)$$

where $\omega_{0x,y}$ are the frequencies of local electron – plasmon resonances, γ is the electron scattering rate in an LENS, ω_c^* is the effective cyclotron frequency, m^* is the effective carrier mass in an LENS, n_s is the average electron surface density in the two-dimensional structure, n_{ds} is the number of LENs per unit area, $N_d = \tilde{n}_s W_x W_y$ and \tilde{n}_s are the number of electrons and the average electron number density in one LENS, respectively, $W_{x,y}$ are the characteristic sizes of a (rectangular) LENS, and d^* is the effective thickness of the two-dimensional system (in the case of a bilayer LENS [43, 45]).

Because the two-dimensional dynamic conductivity of an STDES, formula (24) with $B = 0$, has a frequency dependence similar to that of the two-dimensional layer of a polar semiconductor, Eqns (21) and (23), it follows from formulas (22)–(27) that in the absence of an external magnetic field the resonant reflection from an STDES similar to that shown in Fig. 6 should be observed near each of the local electron – plasmon resonances. The spectral position, depth, and width of such a resonance are determined by the values of the parameters $\omega_{0x,y}$ and γ , and also by the average electron surface density n_s which determines the effective ‘oscillator strength’ of the resonance. In particular, the two-dimensional concentration of LENs influences only the depth and width, but not the spectral positions of transmission minima (reflection maxima) [46]—a fact which Eqns (22)–(27) do incorporate because reducing the two-dimensional concentration of LENs results in decreasing the oscillator strength n_s virtually without changing its resonance frequency $\omega_{0x,y}$ and the damping parameter γ . In the limit of zero damping of optical phonons (or electrons) in the local structure, the conditions $r^{(x,y)} = -1$, $t^{(x,y)} = 0$ should be satisfied at a reflection resonance for the arbitrarily small (down to monatomic) physical thickness d (or d^*) of the 2D system (23) or (24).

On the other hand, formulas (22) suggest that in the case of $\sigma_{xx,yy} = 0$ (and $\sigma_{xy} = 0$, $B = 0$) an STDES at the boundary of dissimilar media with $\varepsilon^{(1)} < \varepsilon^{(2)}$ becomes optically transparent for a photon with appropriate polarization. The photon transmission and reflection coefficients are the same as at the interface of media 1 and 2 without a 2D electronic system. Reference [48] described the total transmission of a photon through a thin semiconductor layer made of high-permittivity material and containing a two-dimensional electron gas. In the recent paper [49], a similar phenomenon of a ‘totally transparent structured film’ was discovered experimentally in the optical range in a two-dimensional square lattice fabricated from pairs of cylindrical gold posts ≈ 80 nm in height placed on a glass substrate. Within the framework of Eqns (22)–(28) and expression (24) for $\sigma_{xx,yy}$, this phenomenon can be described, for example, by taking $\sigma_{xx} = 0$, $d^* \sim 80$ nm, $\bar{\varepsilon} - \varepsilon^{(1)} \approx 0.63$ (vacuum–glass interface), $m^* = m_e$, $B = 0$, and the corresponding values of the electron–plasmon resonance frequency ω_{0x} , electron scattering parameter γ , and the average electron surface density n_s .

The essential point is that to explain the experimental results of Ref. [49] in terms of Eqns (22)–(28) and using the photon analogy of the Fano effect, there is no need to introduce (as in Ref. [49]) negative permeabilities $\mu(\omega)$ in the optical frequency range. In Ref. [49] and also in Refs [44–46], the negative values of permeability in the optical frequency range were used to explain the resonant enhancement in photon reflection from STDESs. (In this connection, interestingly, earlier references on the reflection of electromagnetic waves from STDESs [43] did not use negative permeabilities of the system to explain experiments.) Indeed, Eqns (22)–(28) assume that the permeability of a nonmagnetic STDES (including when in an external magnetic field) is identically equal to unity. These equations can also be used to describe the resonant enhancement in photon reflection from an STDES (see Fig. 6). (According to formulas (23), (24), and (27), coating a 2D system of pairs of nanoposts with a thin layer of glycerine of thickness $d^{(3)} \sim d^*$ and with $\varepsilon^{(3)} > 1$ [49] increases the average effective dielectric constant $\bar{\varepsilon}$ at the interface and lowers the frequency ω_{0x} of the reflection resonance from an STDES—which is exactly what the experiments in Ref. [49] showed.) Moreover, in accordance with the estimates given by Landau and Lifshitz [50] and discussed in Ref. [49], taking into account the deviation of $\mu(\omega)$ from unity in the optical and higher-frequency ranges is “clear excess of accuracy”. Therefore, an important conclusion of this section is that the resonant enhancement in photon reflection from STDESs found experimentally in the optical frequency range can be explained by and reproduced with equations like (22)–(28) under the assumption of the permeability of the system being identically equal to unity, $\mu(\omega) = 1$, which is fully consistent with the statement in Ref. [50] concerning the permeability of materials in the optical (and higher) frequency range.

Interest in media with negative permeability $\mu(\omega)$ was sparked by the prediction made by Veselago [51] that *isotropic material* with both negative ε and μ should have a negative refraction index $n = \sqrt{\varepsilon\mu}$, the underlying reason being that in such a material the Poynting vector $\mathbf{P} = (c/4\pi) \mathbf{E} \times \mathbf{H}$ is antiparallel to the photon wave vector \mathbf{k} . Additional interest in these unusual materials was created by the suggestion put forward in Ref. [52] that the materials with negative refraction indices could be used to fabricate ‘perfect lenses’—lenses whose resolving power is not limited by the wavelength of the

photon and which are therefore of much interest. Because materials with such properties do not exist in nature—not as far as optical wavelengths are concerned—extensive efforts have been made to produce artificial materials with both ε and μ being negative [53]. But, as noted above when mentioning the estimate and statement in the book [50], the predicted existence of materials with negative μ in the optical (and higher) frequency range is theoretically inconsistent. On the other hand, no known theoretical framework is at odds with the existence of *anisotropic materials* in which the Poynting vector is not along (or is even antiparallel to) the photon wave vector in a certain frequency range (and in a certain interval of directions) (see, for example, Ref. [54]). Understanding the refraction of waves in such media can be greatly enhanced by analyzing the geometry of the ‘isofrequency surface’ of elementary excitations propagating in an anisotropic medium. One example is given in Ref. [55], in which the amplitude damping of an elastic surface wave in the bulk of an anisotropic crystal is related to the presence of nonconvex portions at the isofrequency surface of crystal phonons with appropriate polarization. Section 5 below briefly describes a simple periodic, anisotropic, acoustic system negatively refracting for a certain acoustic frequency range and suggests some simple experiments in which this property can be observed. The essential point here is that such a periodic anisotropic system can be fabricated either from macroscopic or nanoscale structural elements.

5. Negative refraction of phonons in periodic anisotropic media and the acoustic analogue of the Fano effect

Let us consider a simple two-component acoustic superlattice consisting of plane layers of materials A and B. The propagation of phonons in a periodic medium can be described on the basis of the Bloch waves, in which a wave is characterized by the Bloch wave vector \mathbf{k} , frequency ω and group velocity \mathbf{V}_{ph} . In the quasiclassical approximation, these wave characteristics can change adiabatically in time and space, and in doing so obeying the following equations (see, for example, Ref. [56]):

$$\dot{\mathbf{k}} = -\nabla\omega, \quad \mathbf{V}_{ph} = \frac{\partial\omega}{\partial\mathbf{k}}, \quad (29)$$

where the frequency ω determines the phonon energy $E_{ph} = \hbar\omega$ and is therefore assumed to be positive.

As follows from equations (29), the directions of the phonon group velocity and the corresponding Poynting vector are determined by the direction of the (outer) normal to the phonon isofrequency surface $\omega = \text{const}$. Using the results of Ref. [57] on the propagation of waves at an arbitrary angle to an axis of an acoustic superlattice, it is possible to prove that in a two-component acoustic superlattice formed by layers of thicknesses d_A and d_B of materials with very different acoustic impedances ($\rho_A c_A \ll \rho_B c_B$, where $\rho_{A,B}$ and $c_{A,B}$ are the density and velocity of the sound of the appropriate polarization in layers A and B), in the case of $c_A/d_A = c_B/2d_B$ the second miniband has a small width and a negative group velocity along the Z-axis of the superlattice:

$$\omega^2 = c_A^2 k_x^2 + \left[\pi \frac{c_A}{d_A} + 2 \frac{c_A}{d_A} \frac{\rho_A c_A}{\rho_B c_B} \cos(k_Z d) \right]^2, \quad d = d_A + d_B, \quad (30)$$

$$V_{\text{ph}Z} \approx -2c_A \frac{d}{d_A} \frac{\rho_A c_A}{\rho_B c_B} \sin(k_Z d). \quad (31)$$

Such a relatively narrow miniband is found, for example, in a simple acoustic superlattice formed by Plexiglass layers periodically arranged in water (in which case A and B in formulas (30)–(31) stand for water and Plexiglass, respectively). In a perturbed acoustic Plexiglass–water superlattice, temporal *acoustic Bloch oscillations* in the ultrasound transmission coefficient through the superlattice layer were observed for the first time, similar to electron Bloch oscillations found in a semiconductor superlattice in an external electric field [58]. The perturbation of the acoustic superlattice was achieved by a water layer thickness gradient—leading, in accordance with Eqns (29) and (31), to temporal oscillations in the group velocity (and hence in the acoustic Poynting vector) along the superlattice axis:

$$V_{\text{ph}Z} \approx 2c_A \frac{d}{d_A} \frac{\rho_A c_A}{\rho_B c_B} \sin(\omega_B t), \quad (32)$$

where the frequency $\omega_B = |d\partial\omega_{\text{cav}}/\partial Z| \approx |\pi(c_A/d_A^2)\partial d_A/\partial z|$ of acoustic Bloch oscillations is determined by a small gradient of central resonance frequencies of ‘water cavities’ between neighboring Plexiglass layers, $\omega_{\text{cav}} = \pi c_A/d_A$ [see formula (30)].

Because an unperturbed anisotropic periodic system has a frequency interval for waves with negative group velocity along the superlattice axis—the length of the interval being equal to the width $2\Delta = 4\rho_A c_A^2/(\rho_B c_B d_A)$ of the acoustic miniband (30) near the central resonance frequency ω_{cav} —this simple system makes it possible for ultrasonic acoustic waves to undergo negative refraction and to have a negative refraction index. Some aspects of negative refraction of acoustic waves have been studied in acoustical crystals that are more difficult to make, consisting of a two-dimensional lattice of solid cylinders in the air (see Ref. [59] and references cited therein).

Negative refraction in the three-dimensional layered system under consideration can be conveniently explained by constructing the isofrequency surface of acoustic oscillations using Eqn (30). Figure 7 displays the cross section of this surface by the $k_x k_z$ plane for the parameters of the water–Plexiglass superlattice that were used in the experiments: $d = 2d_A$, $\rho_A c_A/(\rho_B c_B) = 0.47$, and $\omega = 1.15\omega_{\text{cav}}$ [58]. (A miniband with such an isofrequency surface occurs for $\omega > \omega_{\text{cav}} - \Delta$, and for $\omega > \omega_{\text{cav}} + \Delta$ the isofrequency surfaces shown in Fig. 7 transform into a single open surface in the form of a k_z -aligned ‘corrugated cylinder’—a Fermi surface shape known from the theory of metals [60].) In accordance with the laws of radiation, the group velocity of an acoustic wave incident normally to the layers should be directed inward with regard to the superlattice, whereas its wave vector will, according to Eqn (31) and Fig. 7, be directed oppositely, i.e., away from the superlattice. Therefore, if the second edge of the superlattice is cut, making it wedge-shaped, then the acoustic wave going out from the opposite side will be refracted at a negative angle to the external medium. The same phenomenon of negative refraction of electromagnetic waves in microwave range (10 to 12 GHz) was studied in Refs [61, 62] in much more complex wedge-shaped structures with a ‘high density of wires’. The discovery and study of negative acoustic refraction in simple layered

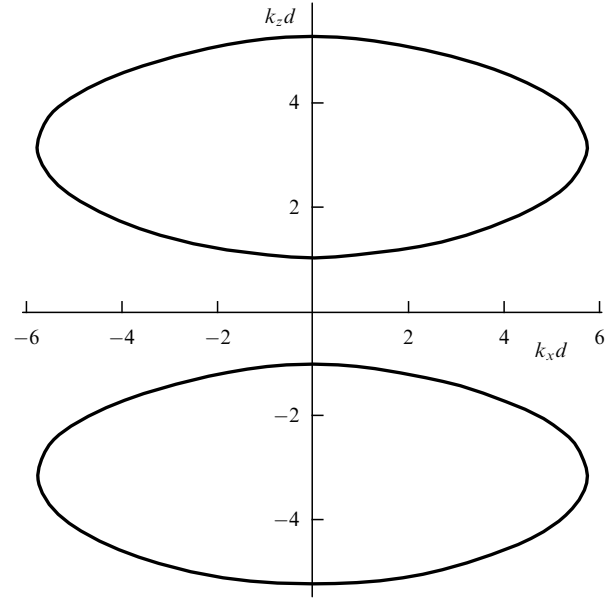


Figure 7. Isofrequency surface of longitudinal ultrasound waves in an acoustic water–Plexiglass superlattice. The frequency and normalized parameters of the superlattice are given in the text.

water–solid systems is potentially of both fundamental and applied interest. It is essential that a composite medium for the study of acoustic Bloch oscillations and negative refraction can be made both of macroscopic elements (like layers of a solid material in water) and of nanoscale structural elements (like the semiconductor superlattice with ‘acoustic nanocavities’ designed in Ref. [1]).

Negative group velocity of waves propagating along an axis of superlattice (31) in miniband (30) will also be encountered in studying acoustic Bloch oscillations in a perturbed superlattice similar to that considered in Ref. [58] but for a different arrangement of the experiment. What needs to be monitored in this new arrangement is the transverse oscillations of a Gaussian beam (with a finite width across layers) propagating along the layers of a perturbed superlattice. A similar arrangement of the experiment was used, for example, in Ref. [63], which studied the transverse Bloch oscillations of an optical Gaussian beam in a two-dimensional system of parallel waveguides with a transverse gradient of refraction indices of individual waveguides (the gradient being due to a transverse gradient in temperature). In the experiments of Ref. [63], a Gaussian beam excited by a laser at the ends of several waveguides periodically shifted to the region of a higher index of refraction as it propagated, the reason being that optical excitations have a positive group velocity along the axis of the unperturbed superlattice. However, in the case of miniband (30) with a negative group velocity (31) along the axis of the unperturbed acoustic superlattice, a Gaussian beam of ultrasound waves which is excited at the ends of several layers will, as it propagates, shift periodically to the region of a lower index of refraction, i.e., to that region of a perturbed superstructure where water layers between Plexiglass layers are thinner. The Bloch oscillations of the transverse shift of the ultrasound Gaussian beam can be visualized.

A further possible source of a narrow acoustic miniband with a negative group velocity along an axis of a superlattice is

an analogue of the Fano effect for acoustic waves in the case in which relatively thin layers of a solid material have holes (with a diameter of about the thickness of the layer) forming identical two-dimensional lattices, square or rectangular, in all the layers of the water–solid superlattice. If the lattice constant a of the two-dimensional lattice of holes exceeds the thickness of the solid material layer, then there is a possibility for a normally incident longitudinal wave to be resonantly reflected from an individual thin layer due to the destructive interference of two acoustic paths: through the resonant oscillations of standing bending waves in a perforated layer (with in-layer wave number $\approx \pi/a$), and through the ‘averaged’ solid material layer. Resonant reflection from a relatively thin perforated layer of a solid material in water will have a line shape similar to that shown in Fig. 6. But if solid material layers with identical two-dimensional lattices of holes form a superlattice and if the narrow transmission resonance falls within the first forbidden band of the superstructure (this position of the resonance of acoustic waves with the bending oscillations of the cylinder shape is investigated in Ref. [33] for a two-dimensional lattice of thin-walled cylinders in a gas or a liquid), then such a resonance can produce in the superlattice a narrow miniband for wave propagation with negative dispersion of the group velocity along a superlattice axis (because such a miniband will be the closest to the acoustic band with the positive dispersion). In this case, the acoustic waves that enter into resonance with the narrow miniband undergo negative refraction when passing through a wedge-shaped sample of such acoustic ‘metamaterial’. The resonant reflection effect was first discovered in a study of photon propagation through layers of a transparent material with a two-dimensional lattice of holes [25, 26]. By analyzing the isofrequency surface of phonons or photons in anisotropic periodic systems whose structural elements show the Fano effect, it is possible to explain the origin of negative acoustic or electromagnetic wave refraction in such media.

6. Conclusion

Let us summarize the main points of this report. (1) A description is given for a theory developed for the phonon analogue of the Fano effect, which is predicted for the first time and is observed in low-dimension multichannel systems, in particular, in ‘locally resonant’ media. (2) A simple model is proposed for an additional channel of transmission of long-wavelength phonons through a crystal two-dimensional defect or a quasi-one-dimensional phonon nanowaveguide. How and when an additional transmission channel for acoustic phonons can lead to the total resonant reflection or absorption of phonons is analyzed. (3) It is shown that the nonresonant interaction of acoustic phonons with the dynamically rough surface of a nanowaveguide markedly reduces the mean free path of phonons in such low-dimension structures. The predicted reduction in phonon mean free path and phonon thermal conductivity of nanowires is in agreement with experimental data on thermal conductivity of silicon nanowires with smooth and rough surfaces. (4) It is shown that the multichannel propagation and scattering of photons can lead to an observed enhancement in reflection from thin layers of polar semiconductors and two-dimensional structured electronic systems on a transparent substrate. Introducing the multichannel scattering of photons in a two-dimensional structured electronic

system makes it possible in some of the cases studied to avoid using the negative permeability at optical frequencies. (5) It is shown that analysis of phonon or photon isofrequency surfaces in macroscopically or nanoscale periodic structures makes it possible to explain the origin of the negative refraction of acoustic and electromagnetic waves in such media and to predict new observable effects.

Acknowledgments. The author is grateful to O V Rudenko, A V Savin, and E S Syrkina for discussions on various aspects of this work. This work was supported by the RFBR grant No. 08-03-00420.

References

1. Huynh A et al. *Phys. Rev. Lett.* **97** 115502 (2006)
2. Strocio M A et al. *J. Phys.: Condens. Matter* **8** 2143 (1996)
3. Feher A et al. *Fiz. Nizk. Temp.* **31** 1211 (2005) [*Low Temp. Phys.* **31** 921 (2005)]
4. Li D et al. *Appl. Phys. Lett.* **83** 2934 (2003)
5. Hochbaum A I et al. *Nature* **451** 163 (2008)
6. Boukai A I et al. *Nature* **451** 168 (2008)
7. Padgett C W, Shenderova O, Brenner D W *Nano Lett.* **6** 1827 (2006)
8. Fano U *Phys. Rev.* **124** 1866 (1961)
9. Sánchez I, Martín F *Phys. Rev. A* **49** 5116 (1994); *J. Phys. B: At. Mol. Opt. Phys.* **27** 4105 (1994)
10. Piao G et al. *Solid State Commun.* **75** 835 (1990)
11. Cerdeira F, Fjeldly T A, Cardona M *Phys. Rev. B* **8** 4734 (1973)
12. Tejedor C et al. *Phys. Rev. B* **32** 5303 (1985)
13. Bellani V et al. *Semicond. Sci. Technol.* **11** 1411 (1996)
14. Faist J et al. *Nature* **390** 589 (1997)
15. Göres J et al. *Phys. Rev. B* **62** 2188 (2000)
16. Zacharia I G et al. *Phys. Rev. B* **64** 155311 (2001)
17. Kim J et al. *Phys. Rev. Lett.* **90** 166403 (2003)
18. Johnson A C et al. *Phys. Rev. Lett.* **93** 106803 (2004)
19. Sato M et al. *Phys. Rev. Lett.* **95** 066801 (2005)
20. Kobayashi K et al. *Phys. Rev. Lett.* **88** 256806 (2002)
21. Nakanishi T, Terakura K, Ando T *Phys. Rev. B* **69** 115307 (2004)
22. Hofstetter W, König J, Schoeller H *Phys. Rev. Lett.* **87** 156803 (2001)
23. Kosevich Yu A *Solid State Commun.* **104** 321 (1997)
24. Gantounis G, Stefanou N *Phys. Rev. B* **72** 075107 (2005)
25. Fan S, Joannopoulos J D *Phys. Rev. B* **65** 235112 (2002)
26. Suh W, Solgaard O, Fan S J. *Appl. Phys.* **98** 033102 (2005)
27. Kosevich Yu A *Prog. Surf. Sci.* **55** 1 (1997)
28. Fellay A et al. *Phys. Rev. B* **55** 1707 (1997)
29. Brekhovskikh L M *Volny v Sloistykh Sredakh* (Waves in Layered Media) (Moscow: Izd. AN SSSR, 1957) [Translated into English (New York: Academic Press, 1960)]
30. Liu Z et al. *Science* **289** 1734 (2000)
31. Goffaux C et al. *Phys. Rev. Lett.* **88** 225502 (2002)
32. Goffaux C, Sánchez-Dehesa J *Phys. Rev. B* **67** 144301 (2003)
33. Kosevich Yu A, Goffaux C, Sánchez-Dehesa J *Phys. Rev. B* **74** 012301 (2006)
34. Landau L D, Lifshitz E M *Teoriya Uprugosti* (Theory of Elasticity) (Moscow: Nauka, 1987) [Translated into English (Oxford: Pergamon Press, 1986)]
35. Andreev A F, Kosevich Yu A *Zh. Eksp. Teor. Fiz.* **81** 1435 (1981) [*Sov. Phys. JETP* **54** 761 (1981)]
36. Kosevich Yu A, Syrkina E S *Fiz. Tverd. Tela* **33** 2053 (1991) [*Sov. Phys. Solid State Phys.* **33** 1156 (1991)]
37. Dunlap D H, Wu H-L, Phillips P W *Phys. Rev. Lett.* **65** 88 (1990)
38. Phillips P, Wu H-L *Science* **252** 1805 (1991)
39. Kent A J et al. *Phys. Rev. Lett.* **96** 215504 (2006)
40. Mingo N et al. *Nano Lett.* **3** 1713 (2003)
41. Cahill D G, Watson S K, Pohl R O *Phys. Rev. B* **46** 6131 (1992)
42. Born M, Huang K *Dynamical Theory of Crystal Lattices* (Oxford: Clarendon Press, 1954) [Translated into Russian (Moscow: IL, 1958)]
43. Demel T et al. *Phys. Rev. B* **38** 12732 (1988)
44. Yen T J et al. *Science* **303** 1494 (2004)

45. Shalaev V M et al. *Opt. Lett.* **30** 3356 (2005)
46. Linden S et al. *Science* **306** 1351 (2004)
47. Kosevich Yu A *Zh. Eksp. Teor. Fiz.* **96** 353 (1989) [*Sov. Phys. JETP* **69** 200 (1989)]
48. Kosevich Yu A *Pis'ma Zh. Eksp. Teor. Fiz.* **53** 143 (1991) [*JETP Lett.* **53** 150 (1991)]
49. Grigorenko A N et al. *Nature* **438** 335 (2005)
50. Landau L D, Lifshitz E M *Elektrodinamika Sploshnykh Sred* (Electrodynamics of Continuous Media) (Moscow: Nauka, 1952) [Translated into English (Oxford: Pergamon Press, 1984)]
51. Veselago V G *Usp. Fiz. Nauk* **92** 517 (1967) [*Sov. Phys. Usp.* **10** 509 (1968)]
52. Pendry J *Phys. Rev. Lett.* **85** 3966 (2000)
53. Shalaev V M *Nature Photon.* **1** 41 (2007)
54. Hoffman A J et al. *Nature Mater.* **6** 946 (2007)
55. Kosevich A M, Kosevich Yu A, Syrkin E S *Zh. Eksp. Teor. Fiz.* **88** 1089 (1985) [*Sov. Phys. JETP* **61** 639 (1985)]
56. Landau L D, Lifshitz E M *Teoriya Polya* (The Classical Theory of Fields) (Moscow: Nauka, 1988) [Translated into English (Oxford: Pergamon Press, 1983)]
57. Kosevich Yu A, Syrkin E S *Phys. Rev. B* **43** 326 (1991)
58. Sanchis-Alepuz H, Kosevich Yu A, Sánchez-Dehesa J *Phys. Rev. Lett.* **98** 134301 (2007)
59. Lu M-H et al. *Nature Mater.* **6** 744 (2007)
60. Lifshitz E M, Pitaevskii L M *Fizicheskaya Kinetika* (Physical Kinetics) (Moscow: Fizmatlit, 2001) [Translated into English (Oxford: Pergamon Press, 1981)]
61. Shelby R A, Smith D R, Schultz S *Science* **292** 77 (2001)
62. Parazzoli C G et al. *Phys. Rev. Lett.* **90** 107401 (2003)
63. Pertsch T et al. *Phys. Rev. Lett.* **83** 4752 (1999)